Fuel 354 (2023) 129331

Contents lists available at ScienceDirect

Fuel

journal homepage: www.elsevier.com/locate/fuel

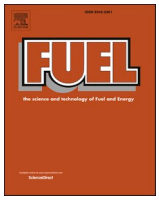

Full Length Article

Laminar burning velocities and Markstein numbers for pure hydrogen and methane/hydrogen/air mixtures at elevated pressures

Marwaan AL-Khafaji [a], Junfeng Yang [a,*], Alison S. Tomlin [b], Harvey M. Thompson [a], Gregory de Boer [a], Kexin Liu [c], Mohamed E. Morsy [a]

[a] School of Mechanical Engineering, University of Leeds, Leeds LS2 9JT, United Kingdom
[b] School of Chemical and Process Engineering, University of Leeds, Leeds LS2 9JT, United Kingdom
[c] Siemens Energy, Lincoln LN6 3AD, United Kingdom

ARTICLE INFO

Keywords:
Laminar burning velocity
Markstein length
Flame instability
Hydrogen
Cellular flames

ABSTRACT

Spherically expanding flame propagations have been employed to measure flame speeds for H_2/CH_4/air mixtures over a wide range of H_2 fractions (30 %, 50 %, 70 and 100 % hydrogen by volume), at initial temperatures of 303 K and 360 K, and pressures of 0.1, 0.5 and 1.0 MPa. The equivalence ratio (ϕ) was varied from 0.5 to 2.5 for pure hydrogen and from 0.8 to 1.2 for methane/hydrogen mixtures. Experimental laminar burning velocities and Markstein numbers for methane/hydrogen/air mixtures at high pressures, which are crucial for gas turbine applications, are very rare in the literature. Moreover, simulations using three recent chemical kinetic mechanisms (Konnov-2018 detailed reaction, Aramco-2.0-2016 and San Diego Methane detailed mechanism (version 20161214)) were compared against the experimentally derived laminar burning velocities. The maximum laminar burning velocity for 30 % and 50 % H_2 occurs at $\phi = 1.1$. However, it shifts to $\phi = 1.2$ for 70 % H_2 and to $\phi = 1.7$ for a pure H_2 flame. The laminar burning velocities increased with hydrogen fraction and temperature, and decreased with pressure. Unexpected behaviour was recorded for pure H_2 flames at low temperature and $\phi = 1.5$, 1.7 wherein u_l did not decrease when the pressure increased from 0.1 to 0.5 MPa. Although, the measurement uncertainty is large at these conditions, the flame structure analysis showed a minimum decline in the mass fractions of the active species (H, O, and OH) with the rise in the initial pressure. Markstein length (L_b) and Markstein number (Ma_b and Ma_{sr}) varied non-monotonically with hydrogen volume fraction, pressure and temperature. There was generally good agreement between simulations and experimentally derived laminar burning velocities, however, for experiments of rich-pure hydrogen at high initial pressures, the level of agreement decreased but remained within the limits of experimental uncertainty.

1. Introduction

The concept of adding hydrogen to natural gas is growing in popularity, as a means of reducing overall CO_2 emissions where the hydrogen is produced from renewable electricity sources such as solar and wind energy. Natural gas still contributes substantially to power production as the main gas turbine fuel, even though renewable energy sources are growing rapidly globally [1]. Hydrogen can be produced at the time of excess energy or low energy prices (H_2-energy storage) and potentially used in gas turbines during periods of higher energy prices [2]. It thus offers a means of energy storage. It is therefore important to understand the combustion behavior of hydrogen/natural gas mixtures in order to design efficient and low pollutant gas turbines that could potentially operate using mixtures as well as high hydrogen volumes.

Often, methane (CH_4) is used to demonstrate the combustion behavior of natural gas [3], as it occupies around 80–95 % of natural gas components by volume [1]. It has been shown that mixing hydrogen with methane increases the flame speed and extends the flammability limits by increasing the maximum allowable strain rate before flame extinction [4–6]. Sankaran and Hong [7] reported that adding hydrogen to methane enhanced the resistance to strain-induced extinction and consequently increased flame stability. In addition, the gas turbine's ability to operate at a low load can be extended, resulting in an increased feasible load profile [2,8].

Although the flow is turbulent in practical applications, the laminar burning velocity (u_l) is a fundamental parameter used in the design and optimization of gas turbine burners [9–11]. In this study, the

* Corresponding author.
E-mail address: J.Yang@leeds.ac.uk (J. Yang).

https://doi.org/10.1016/j.fuel.2023.129331
Received 5 June 2023; Received in revised form 24 July 2023; Accepted 27 July 2023
Available online 3 August 2023

Nomenclature

A	Flame surface area (m^2)
C_p	Specific heat (kJ/Kg.K)
D	Thermal diffusivity (m^2/s)
L_b	Flame speed Markstein length (mm)
Le	Lewis number
Ma_b	Flame speed Markstein number
Ma_{cr}	Curvature Markstein number
Ma_{sr}	Strain Markstein number
P_u	Initial pressure (MPa)
P_r	Prandtl number
r	Flame radius from Schlieren images (mm)
r_{cl}	Critical flame radius (mm)
S_n	Stretched flame speed (m/s)
S_s	Un-stretched flame speed (m/s)
u_l	Un-stretched laminar burning velocity (m/s)
T_b	Adiabatic equilibrium burned gas temperature (K)
T_u	Unburned gas temperature (K)
U_f	The uncertainty weight factor

Greek symbols

α	Flame stretch rate (1/s)
δ_l	Flame thickness (mm)
k	Thermal conductivity (kJ/m.K.s)
μ	Dynamic viscosity (kg/m.s)
ν	Kinematic viscosity (m^2/s)
φ	Equivalence ratio
ρ_b	burned gas density (kg/m^3)
ρ_u	Un-burned gas density (kg/m^3)

Table 1
A comparison between the present experimental conditions (equivalence ratio, unburned gas pressure and temperature) and previous outward flame propagation studies.

References	% H_2 by volume	P_u (MPa)	T_u (K)	ϕ
[11]	0, 10, 20, 30, 40, 50, 60, 70, 80, 90, 100	0.1	303	*for H_2/CH_4 0.6–1.4 **for pure H_2 0.6–4.5
[19]	0, 20, 40, 60, 80, 100	0.1, 5, 7.5	303, 373, 443	0.8
[20]	0, 10, 30, 50, 70, 90, 100	0.1	350	0.8, 1, 1.2
[26]	100	0.1, 0.5, 1.0	365	0.4, 0.5, 0.6, 0.7, 0.8, 0.9, 1
Present study	30, 50, 70, 100	0.1, 0.5,	303	*for H_2/CH_4 0.8, 0.9, 1, 1.1, 1.2 **for pure H_2 0.5, 0.8, 1, 1.5, 1.7, 2, 2.5
Present study	30, 50, 70, 100	0.1, 0.5, 1.0	360	*for H_2/CH_4 0.8, 0.9, 1, 1.1, 1.2 **for pure H_2 0.5, 0.8, 1, 1.5, 1.7, 2, 2.5

terminology, laminar flame speed, S_n, refers to the flame movement into the space, while the laminar burning velocity, u_l, refers to the speed of the unburned gas moving into the flame. The experimentally derived laminar burning velocities are used to validate chemical mechanisms that could be used within design simulations as well as providing data from which to derive turbulent burning velocities. Therefore, a deep analysis of the laminar flame under gas turbine conditions becomes essential in designing a multi-fuel gas turbine combustor. Various experimental techniques exist to determine (u_l), including flat-burner flames, counter flow/stagnation flames, and outwardly propagating spherical flame-based methods. The latter is the most effective method for deriving laminar burning velocities at elevated pressures of relevance to gas turbine conditions [12]. Moreover, spherical flame propagations provide controlled experiments with a well-defined stretch rate and a simple flame configuration [11,13].

Previous studies [11,14,15] have shown that laminar burning velocities increase when adding hydrogen to methane, as hydrogen has important thermal and chemical effects. Firstly, hydrogen increases the adiabatic flame temperature for the fuel. Secondly, the hydrogen supplies active radicals (H, O, OH) to the reaction [7,16,17]. Mandilas et al. [18], Hu et al. [19] and Okafor et al. [20] used Schlieren photography to determine the laminar burning velocities of methane/hydrogen mixtures in a cylindrical combustion chamber at various hydrogen volume fractions. They concluded that the un-stretched laminar burning velocities increase significantly as the hydrogen fraction increases. The same conclusion was made by Wang et al. [21], who conducted an experimental study to derive the laminar burning velocities of methane/hydrogen/air mixtures in a flat flame burner, at constant fuel and air mass flow rates.

Hu et al. [19] conducted research with hydrogen volume fractions varying from 0 to 100 %. They concluded that the laminar burning velocity increased linearly with temperature but decreased when the initial pressure was increased. Research on laminar burning velocities for pure hydrogen is well known [22–25], however, the measurement of the un-stretched laminar burning velocity for mixtures with high hydrogen volumetric fraction at high initial pressures ($P_u \geq 0.5$ MPa) is very challenging due to the presence of flame cellularity in the early stages of flame propagation, which results from the Darries-Landau and thermo-diffusive instabilities [26]. At these conditions, there are no data that can be used for extrapolation to obtain the laminar burning velocity. Consequently, Bradley et al. [26] used the linear instability theory of Bechtold and Matalon [27] and the fractal theory of Bradley [28] to expand the stable regime and extrapolate it to zero stretch rate to obtain the unstretched laminar burning velocities for lean hydrogen at high initial pressure. This method [27] has been recently adapted to obtain the laminar burning velocities and examine pure hydrogen's flame cellularity at high pressures [29]. However, this method includes empirical constants that may not be suitable for the wide range of initial conditions and equivalence ratios needed to explore the laminar burning velocity.

As shown in Table 1, a small number of previous experimental studies have focused on laminar burning velocities for methane/hydrogen mixtures at high pressures, which are crucial for gas turbine applications [30]. Previous studies have determined laminar burning velocities in small-volume vessels, with volumes of 5 L [11,19] and 3.5 L [20], which could have strong wall-confinement effects and limited field of view. Therefore, researchers in [11,19,20] had to extrapolate the data of the flame radius up to 25 mm to reduce the effect of the pressure increase and wall confinement on the measurements. In order to avoid the disadvantages of small combustion vessels, a large spherical vessel (30 L) is used in the present study to investigate hydrogen/methane flame propagation at nearly constant pressure, thus providing data (laminar burning velocities and Markstein numbers) of relevance to practical gas turbines. In this large vessel, the flame propagation was recorded up to 75 mm flame radius while pressure fluctuations remained small.

Using spherical outward flame propagation, Hu et al. [11] derived laminar burning velocities for pure hydrogen and methane/hydrogen

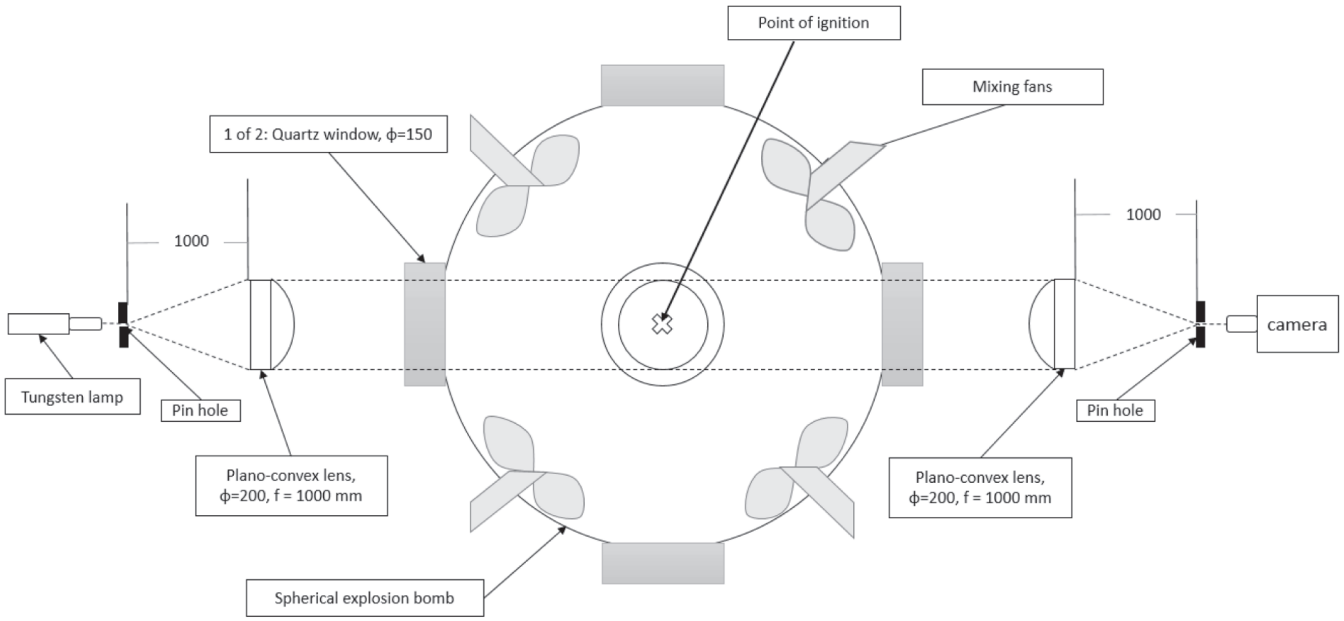

Fig. 1. Schematic view of the vessel and auxiliary system, for Schlieren optical configuration.

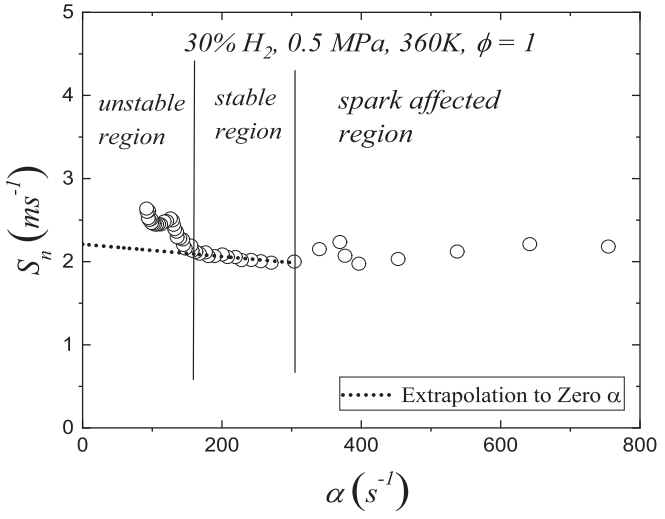

Fig. 2. Flame speed *vs.* flame stretch rate for 30 % H_2 in CH_4 by volume at 0.5 MPa, 360 K, $\phi = 1$.

mixtures, but only for atmospheric conditions. Following their initial study, Hu et al. [19], explored methane/hydrogen mixtures at pressures up to 0.75 MPa, but the equivalence ratio (ϕ) was only 0.8, limiting its applicability since the air–fuel ratio varies over a wide range in practical combustors, such as gas turbine combustors, industrial furnaces and aviation engines [31]. Therefore, the current paper aims to fill the research gap by providing laminar burning velocities and Markstein numbers for lean and rich methane/hydrogen mixtures at high pressures.

In laminar pre-mixed flame propagation, the stretch rate and flame surface cellularity must be reported with the associated Markstein number. The stretch rate and the onset of instability determine the unstretched laminar burning velocities and Markstein number (Ma_b) [32]. Ma_b is a dimensionless number which quantifies the effect of flame stretch rate upon the laminar flame speed [32]. A small value of Ma_b indicates that the flame stretch rate has only a minor effect on the flame speed. For positive Ma_b, the flame speed decreases with increasing flame stretch rate. In contrast, a negative Ma_b value is accompanied by the early onset of cellularity and flame speeds that increase with increasing stretch rate [19,33]. In order to present complete quantitative studies on laminar flame characteristics, Markstein numbers, flame instabilities and stretch rates must be reported alongside the laminar burning velocities.

The main objective of the present study is to provide experimentally derived laminar burning velocities and Markstein numbers for a wide range of methane-hydrogen-air mixtures at elevated initial pressures up to 1.0 MPa. Hydrogen fraction is varied from 30 % to 100 % (by volume) at two different initial temperatures, 303 K and 360 K. The equivalence ratio was varied from 0.5 to 2.5 for pure hydrogen and from 0.8 to 1.2 for methane/hydrogen mixtures. The experimental data will be useful for kinetics researchers and gas turbine designers who can use the laminar burning velocities and Markstein numbers at these conditions. The paper is organized as follows. Section 2 includes a description of the experimental setup. Section 3 presents the main experimental results and discussion, and Section 4 compares the experimentally-derived laminar burning velocities against numerical predictions from three recently developed kinetic mechanisms for methane/hydrogen oxidation (the San Diego (version 20161214) [34,35], the Konnov-2018 [30] and the Aramco-2.0-2016 [36] reduced mechanisms). Finally, conclusions are drawn in Section 5.

2. Experimental apparatus

A Schlieren technique was employed to measure the flame speed, from which the laminar burning velocities were derived, in a 30 L spherical stainless steel combustion vessel (Leeds MK-II fan-stirred vessel) [37]. The vessel has an internal dimeter of 380 mm, and can withstand initial pressures up to 1.5 MPa and temperatures up to 600 K. It is equipped with three-pair orthogonal quartz windows (diameter of 150 mm) for optical access. The air and fuel are mixed by four fans, which are directly coupled to 8 kW three-phase electric motors with

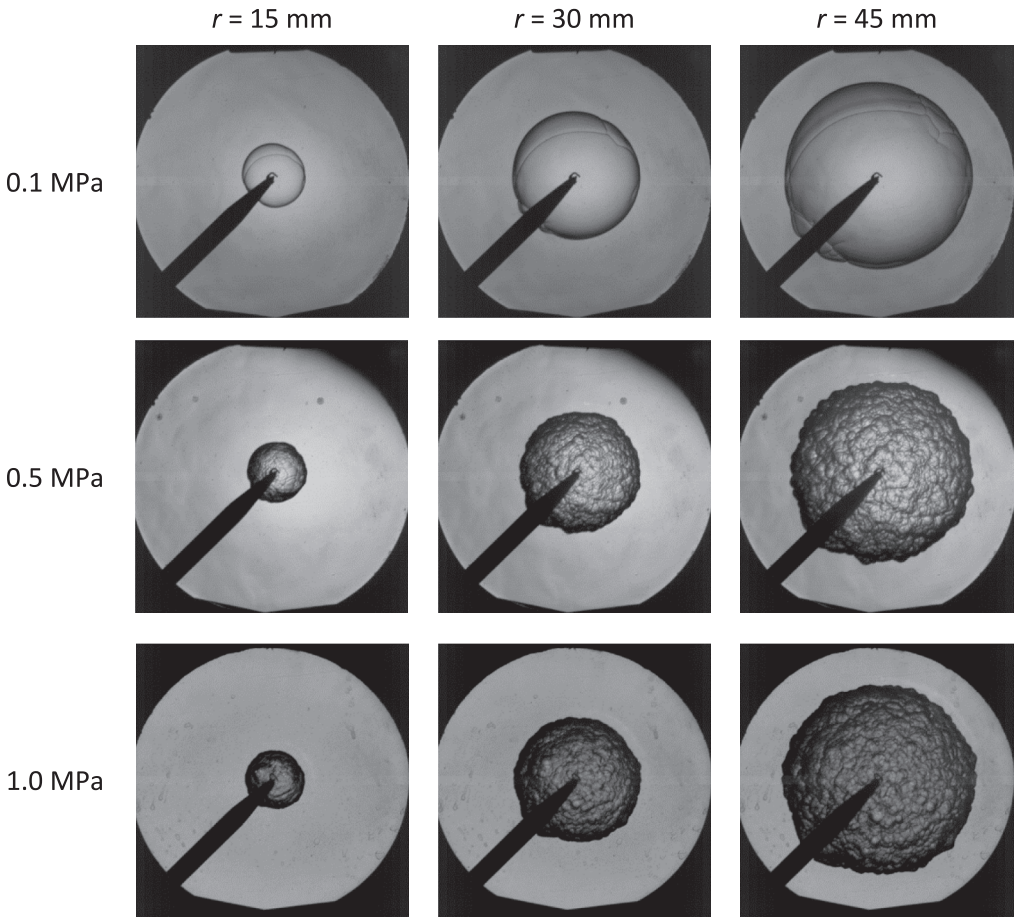

Fig. 3. Flame image for 50 % H_2, $\phi = 0.9$ at 360 K with different pressures.

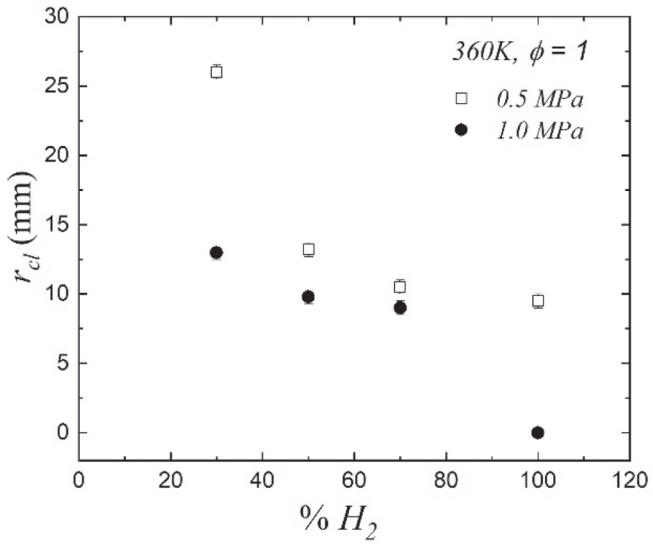

Fig. 4. Critical flame radius (mm) *vs.* volumetric hydrogen fractions at 360 K and $\phi = 1$.

separate speed controllers. The fuel and air were pre-mixed inside the combustion vessel before conducting the experiments. During mixture preparation, the fans were employed to improve mixing and to generate a turbulent flow which enhances the convective heat process and spreads the heat uniformly throughout the chamber. They were switched off prior to ignition and a 15 s time period was allowed, to ensure a full decay of turbulence and to allow the mixture to equilibrate and become quiescent. The vessel is also equipped with two 2 kW heaters to heat up the mixture to the required initial operating temperature. The pressure is measured during the combustion by a Kistler 701A pressure transducer. The temperature is measured by a K type thermocouple [38]. There is a stainless steel/ceramic sparkplug at the vessel's centre, with an adjustable gap from 0.4 to 1.2 mm, to initiate the ignition. The spark plug is connected to an ignition coil system with an adjustable voltage from 10 to 30 V. During the experiments, the ignition energy is maintained at approximately 0.4 mJ to reduce the effect of the spark plasma on the flame velocity measurement [32].

Flames images were obtained using Schlieren ciné-photography (Fig. 1). A 20 W tungsten element lamp is used to generate the light, which expands onto a plano-convex lens with 1 m focal length to collimate a 0.15 m beam through the combustion vessel. The beam then passes through another plano-convex lens which focuses the beam onto a variable diameter iris of 3 mm (pinhole). The Schlieren images are captured using a high-resolution Phantom ultra-high-speed UHS-12, model v2512, CCD camera.

The camera frame rate was varied from 3,000 fps to 30,000 fps, depending on the hydrogen fraction in the mixture. Low speeds were used for 30 % H_2 mixtures at high pressure, as this flame propagates slower than those with higher H_2 fractions. As the flame speed increased, the frame rate was also increased to obtain an appropriate number of images in each case (around one image per 1–1.5 mm of flame movement). The camera pixel was fixed to 512 × 512 pixels with a pixel size of 0.265 mm. More details about the spherical bomb and auxiliary systems can be found in [38,39].

The mixture was prepared in the vessel for the targeted equivalence ratio by adding a specified amount of air or fuel at the required partial

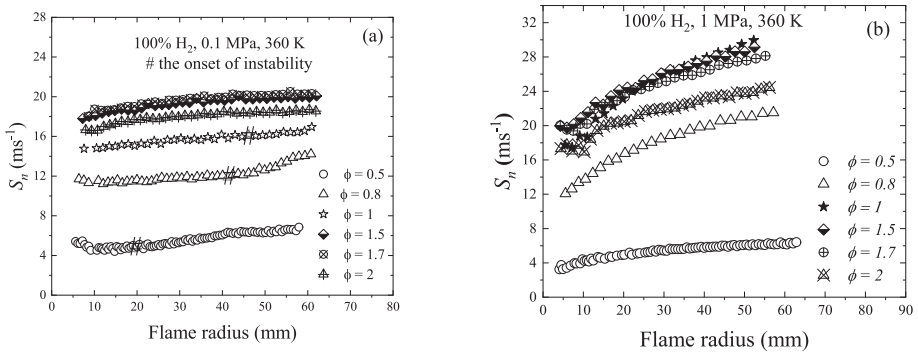

Fig. 5. Flame speed (ms^{-1}) *vs.* flame radius (mm) for pure hydrogen at a) 0.1 MPa, b) 1 MPa with different equivalence ratios.

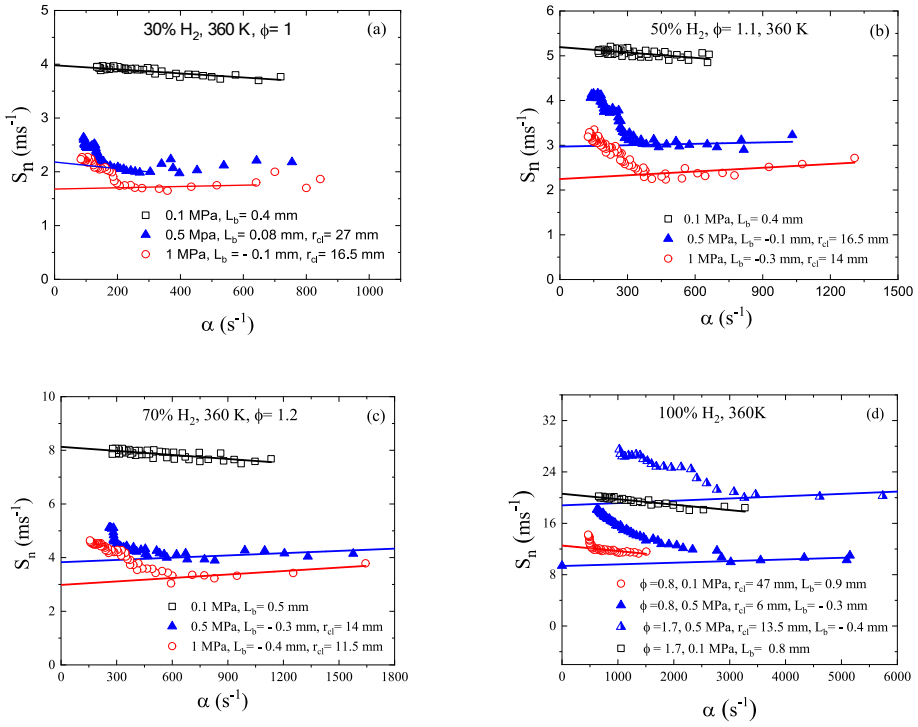

Fig. 6. Flame speed (ms^{-1}) *vs.* stretch rate (s^{-1}) for 30, 50, 70, and 100 % volumetric fraction of hydrogen, for different initial pressures and equivalence ratios.

pressure. The following equations [19] were used to obtain the partial pressure in the mixture preparation:

$$(1-X_{H_2})CH_4+(X_{H_2})H_2+\left(\frac{2}{\phi}(1-X_{H_2})+\frac{X_{H_2}}{2\phi}\right)(O_2+3.762N_2) \quad (2.1)$$

$$P_{H_2}=\frac{X_{H_2}}{\left[1+\left(\left(\frac{2.38}{\phi}\right)(4X_{CH_4}+X_{H_2})\right)\right]}*P_u \quad (2.2)$$

$$P_{CH_4}=\frac{X_{CH_4}}{\left[1+\left(\left(\frac{2.38}{\phi}\right)(4X_{CH_4}+X_{H_2})\right)\right]}*P_u \quad (2.3)$$

$$P_{air}=P_u-P_{CH_4}-P_{H_2} \quad (2.4)$$

P_{H_2}, P_{CH_4} and P_{air} are the partial pressures of hydrogen, methane and air, respectively, P_u is the targeted mixture initial pressure (0.1, 0.5 and 1 MPa), X_{H_2} and X_{CH_4} are the mixture volume fractions of hydrogen and methane, respectively, and ϕ is the mixture equivalence ratio.

After each experiment, the vessel was flushed with dry air and evacuated twice to remove the flue gases. Dry lab air (O_2:N_2) with a ratio of 21:79 % by mole was used in the experiments. Methane and hydrogen high-pressure cylinders were used with a purity of 99.995 %. The fans were run at a low speed (400 rpm) during the mixture preparation to ensure full mixing and uniform temperature. The fans were switched off for at least 60 s before the ignition to bring the mixture to quiescence. A previous study using the same vessel estimated the precision in equivalence ratio to be ±0.04 in the value of ϕ [14]. The experiments were repeated three times at each condition and average values were used in the present data. Reported error bars represent one standard deviation: the sum of squared deviations divided by the number of data points minus one.

Images were processed using a MATLAB code developed in previous studies [38,40,41]. Flame edges are specified in the code to identify the burned and unburned regions. The unburnt gas part of the image is subtracted and remained black, and the flame image relating to the burnt gases is white. The flame area is then calculated by counting the number of pixels of the white region, and an equivalent flame radius, r, is computed from this area by assuming a smooth circular image with the same area. Finally, the time step (dt) is calculated as 1/camera frame rate. The flame propagation speed, S_n, is then determined as:

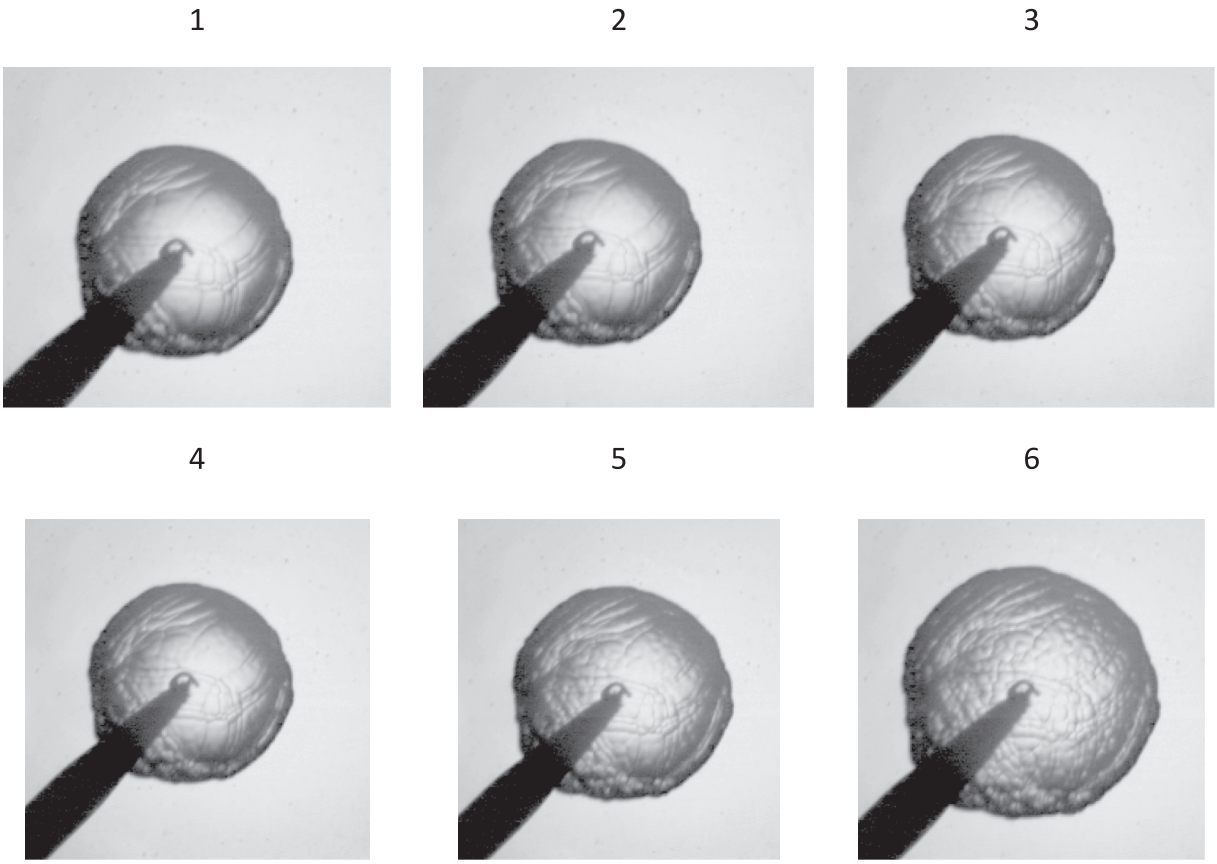

Fig. 7. Possible onsets of instability for the case with 50 % H_2, 0.5 MPa, 360 K and $\phi = 1$.

$$S_n = \frac{dr}{dt} \tag{2.5}$$

where r is the Schlieren flame front radius and t is the time.

Flame stretch rate (α) influences the laminar flame speed, as it affects the species concentration and temperature gradients in the preheat and reaction zones [9,42]. Thus, the stretch effect needs to be eliminated to obtain the unstretched laminar burning velocities [12]. Williams expressed the overall stretch rate as the change in flame surface area divided by the area [43]. The flame stretch rate α is written as:

$$\alpha = \frac{1}{A}\frac{dA}{dt} = \frac{2}{r}S_n \tag{2.6}$$

where A is the area of the spherical flame.

Flame speed (S_n) is plotted against stretch rate (α) for an example case in Fig. 2. The stretched flame speed is extrapolated to zero stretch rate to obtain the unstretched flame speed (S_s). The data in the S_n-α plot is classified in three categories [32]: (i) the region where ignition energy affected the flame, which is eliminated from the extrapolated data. The spark effect continues up to 10 mm flame radius at atmospheric pressure [32] and to 5 mm at high pressure experiments [19]; (ii) the stable region (quasi-steady flame) which is used in the extrapolation to derive the un-stretched flame speed S_s, and (iii) the unstable regime which starts after the onset of cellularity at a critical flame radius (r_{cl}), where the flame speed increases rapidly because of the high flame surface area [33]. The linear relationship between flame speed and stretch rate is expressed in the following equation:

$$S_s - S_n = \alpha L_b \tag{2.7}$$

where L_b is the Markstein length, which is the slope of the line used to extrapolate the stable data to zero stretch rate.

The Markstein length is normalized by flame thickness (δ_l) to obtain the burned gas Markstein number, Ma_b.

$$Ma_b = \frac{L_b}{\delta_l} \tag{2.8}$$

The Markstein number Ma_b is widely used to quantify the effect of the flame stretch rate on the laminar burning velocity [33]. However, there are two contributions of stretch rate; (i) due to flow strain rate, and (ii) due to flame curvature stretch [44]. These effects are quantified by strain Markstein number Ma_{sr} and curvature Markstein number, Ma_{cr}. They are derived from L_b and u_l using the method of Bradley et al. [44]. Previous co-workers [33] highlighted the importance of Ma_{sr} in practical turbulent applications, as it quantifies the effect of aerodynamic strain on the burning rate in outwardly propagating flames [41]. Ma_{sr} is also useful for analyzing quench effects in turbulent combustion [44]. Moreover, Ma_{sr} is larger than Ma_{cr} ($Ma_{sr} \approx 5Ma_{cr}$) in outwardly propagating flames [33,44,45]. Therefore, the present study focuses on L_b, Ma_b and Ma_{sr}.

In the current work, the theoretical method proposed by Bradley et al. [44] has been employed to derive Ma_{sr} and Ma_{cr} from an outwardly propagating spherical flame. The linear dependency of S_n on α enables u_l and L_b to be evaluated from Eq. (2.7). Then the values of L_c and L_s are found from ($u_l - u_n = L_s\alpha_s + L_c\alpha_c$), using multiple regression, as described in [44]. Values of L_{cr} and L_{sr} are derived from Eq. (2.9) as ($L_{sr} = (L_b - L_s)(1/(\rho_u/\rho_b) - 1)$) and $L_{cr} = (L_b - L_c)(1/(\rho_u/\rho_b) - 1)$ and finally the normalisation of these Markstein lengths by the flame thickness yields the corresponding Markstein numbers.

$$u_l - u_{nr} = L_{sr}\alpha_{sr} + L_{cr}\alpha_{cr} \tag{2.9}$$

From mass conservation across the flame front, considering an idealized one dimensional planar flame, the un-stretched laminar burning velocity, u_l, is calculated from [32]:

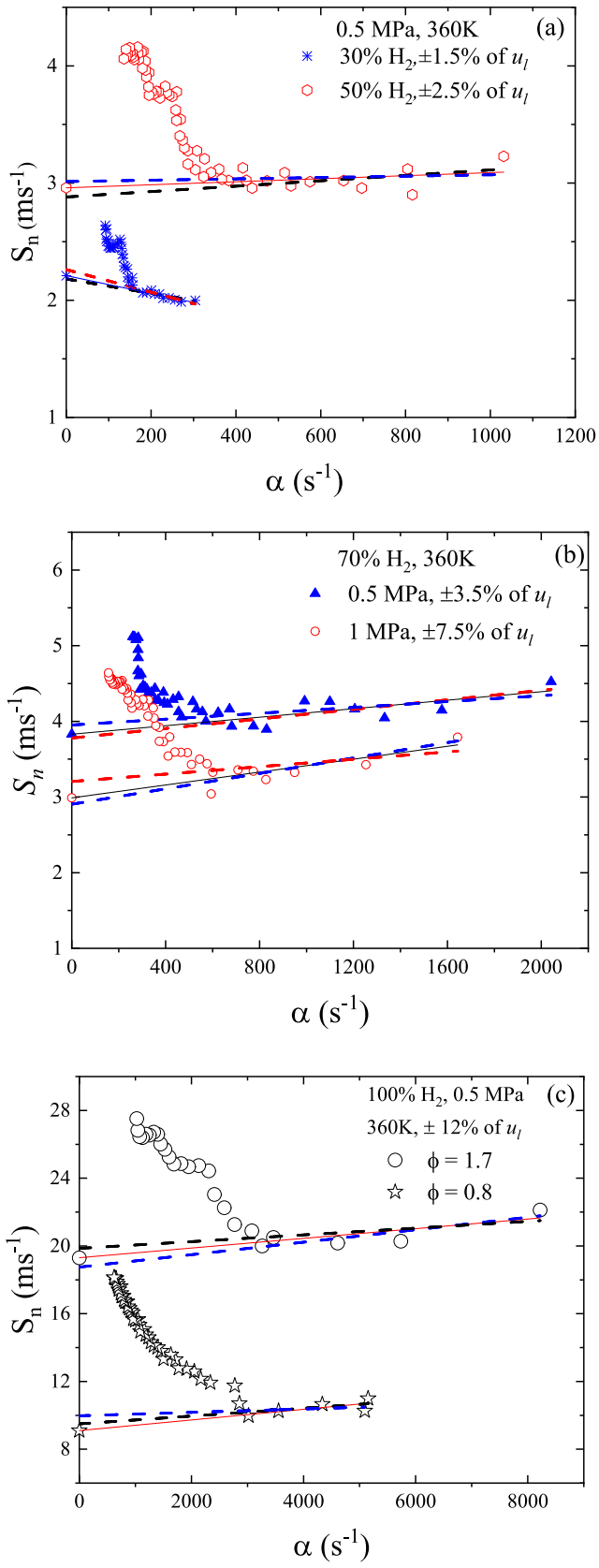

Fig. 8. The measurement uncertainty in the laminar burning velocity due to the choice of the onset of instability condition (a) 30 & 50 % H_2 (b) 70% H_2 and (c) 100% H_2.

$$u_l = \frac{\rho_b}{\rho_u} S_s \tag{2.10}$$

where ρ_u is the unburned gas density at the initial gas temperature (T_u) and ρ_b is the burned gas density at the adiabatic temperature (T_b) assuming that the flame is adiabatic at zero stretch rate [11,32,45]. The chemical equilibrium program, GASEQ [46] was employed for calculating the gas properties at the given temperature and pressure.

The extrapolation method and the selected experimental data used for extrapolation are a source of uncertainty in the derived unstretched laminar burning velocities. The uncertainty in the extrapolation approach is largely dependent on the Lewis number and the normalized stretch rate (Karlovitz stretch number) [12]. The extrapolation approach is based on asymptotic analysis, used for Lewis numbers close to 1 ($L_b \rightarrow 0$) [12,44]. The linear extrapolation method (Eq. (2.7) has been adopted in many studies for hydrogen/methane/air mixtures [11,19,20,26]. However, non-linear extrapolation is used for large carbon-content fuels such as n-butane and n-heptane, which have a large Lewis number ($Le >$ 1) in lean mixtures [47]. Therefore, the present study adopted the linear extrapolation method, with the uncertainty quantified using the correlation of Wu et al. [12]:

$$U_f = Ma_{bLinear} Ka_{mid} = \frac{2L_b}{R_{fmid}} \tag{2.11}$$

where U_f is the uncertainty weight factor, $Ma_{bLinear}$ is the Markstein number from the linear extrapolation, Ka_{mid} is the Karlovitz number in the middle of the extrapolated data (stretch rate normalized by flame thickness), L_b is the Markstein length and $R_{f\,mid}$ is the flame radius in the middle of the extrapolated data. According to Wu et al. [12], (i) the uncertainty in the extrapolation is negligible (±5 %) for $-0.05 < U_f <$ 0.15, (ii) for $U_f <$ -0.05, both linear and nonlinear extrapolation over-predict the un-stretched flame speed, (iii) for $U_f >$ 0.15, extrapolation under-predicts the un-stretched flame speed. Flame thickness, δ_l, is defined as the distance between the end of the cold reactant zone to the beginning of the product zone [45]. However, accurate determination of δ_l is challenging as these zones have rapid heat and mass transfer. This problem is more significant in hydrogen flames, as H radicals in the reaction layer diffuse upstream and are consumed by reaction with O_2 as well as with HCO, CH_2O and CH_4. Consequently, the preheat zone is not chemically inert [48]. Different methods have been adopted in the literature to calculate the flame thickness. The thermal flame thickness [43] is commonly derived from the temperature profile of the flame structure:

$$\delta_l = \frac{(T_b - T_u)}{\left(\frac{dT}{dx}\right)_{max}} \tag{2.12}$$

where T_b and T_u are the adiabatic and unburned gas temperatures, respectively. $\left(\frac{dT}{dx}\right)_{max}$ is the maximum temperature gradient within the flame. The dimensional (or diffusive) laminar flame thickness [10] is defined as the ratio of thermal diffusivity to laminar burning velocity, D/u_l. Substituting D with the viscosity and Prandtl number, the above equation can be re-written as:

$$\delta_l = \frac{\frac{\nu}{u_l}}{P_r} \tag{2.13}$$

where ν is cold mixture kinematic viscosity and Pr is the Prandtl number.

Göttgens et al. [48] evaluated the flame thickness for hydrogen and hydrocarbon fuels by solving the governing equations using detailed chemistry for 1D planar steady premixed flames, and proposed the following expression for the flame thickness δ_l:

$$\delta_l = \frac{\left(\frac{k}{C_p}\right)_{T^o}}{\rho_u u_l} \tag{2.14}$$

where k is thermal conductivity, C_p is mixture specific heat at

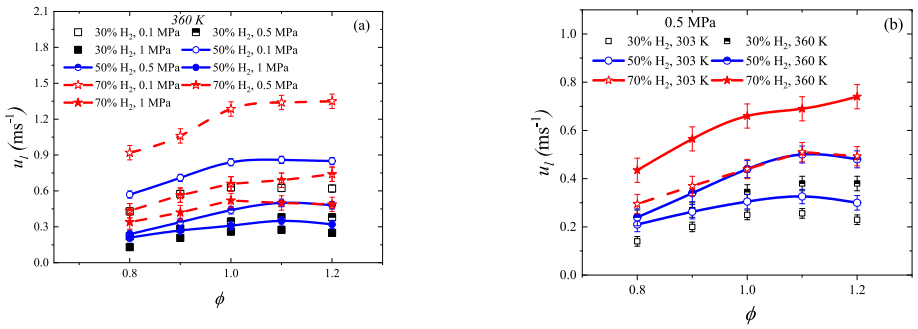

Fig. 9. Un-stretched laminar burning velocity *vs.* equivalence ratio for 30, 50 and 70 % hydrogen fractions at different initial pressures and temperatures (a) at 360 K and different initial pressure, (b) at 0.5 MPa and different initial temperature.

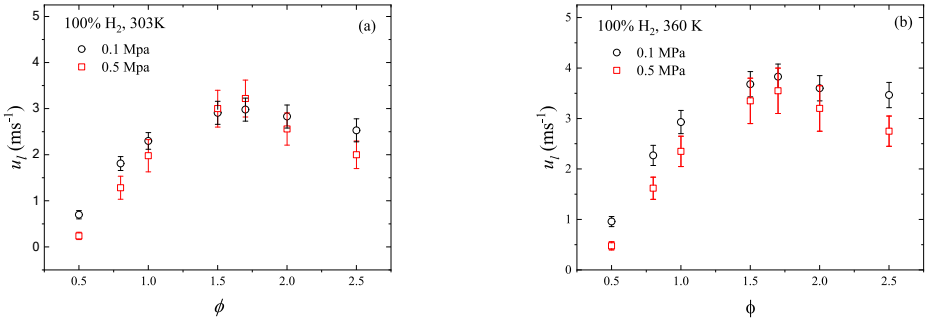

Fig. 10. Un-stretched laminar burning velocity with equivalence ratio for 100 % hydrogen at different initial pressures and temperatures, (a) 303 K and (b) 360 K.

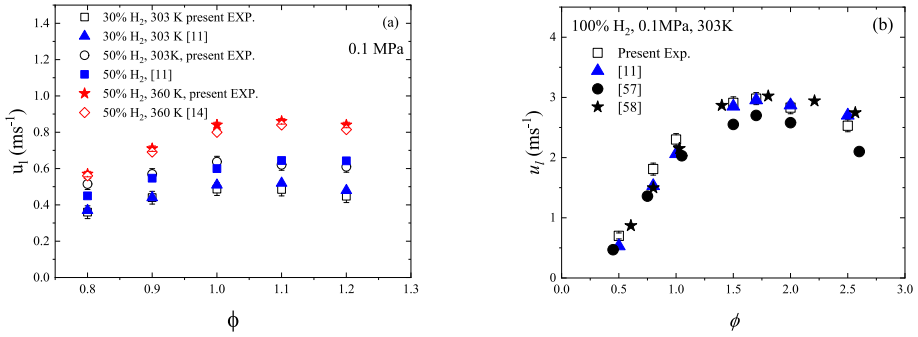

Fig. 11. Un-stretched laminar burning velocity with equivalence ratio for present and previous studies at 0.1 MPa, (a) H_2/CH_4 and (b) pure H_2.

constant pressure, ρ_u is the unburned gas density, and T^o is the critical temperature at which the reaction starts [48]. Following Bradley et al. [40,49,50], Equation (2.14) has been selected to calculate the flame thickness in the present study.

3. Experimental results and discussion

3.1. Flame instabilities

Fig. 3 shows examples of flame front images at different flame radii, *r*, for 50 % hydrogen at 360 K and different pressures. The flame front images are used to identify the transition from the stable to the unstable region. For 50 % H_2 at 0.1 MPa, the flame front is stable, with only a few cracks caused as the flame passes through the spark electrode. This was the case in most low pressure flame propagations except for the lean mixture with 70 % H_2, lean and stoichiometric mixtures with 100 % H_2 in which the flame front was unstable. For high pressure experiments, the flame propagates smoothly in the early stages, as the stretch rate is sufficient to maintain a smooth flame surface. Following this and with a reduction in the stretch rate, cellular instability develops at the critical flame radius (r_{cl}), increasing the flame speed [27,37]. Cracks, which result from ignition effects [33], were shown in the stable flame front. To discriminate between cracked and cellular flames, the flame speed is plotted as a function of flame radius or flame stretch rate. The transition point (i.e. the onset of instability) is located when the flame speed increases significantly.

Interactions between the Darrieus–Landau (DL) and Thermal Diffusion (TD) instabilities are the main cause of cells forming in spherical flame propagations [28,29]. In laminar premixed flames, the competition between heat conduction from the flame and reactant diffusion towards the flame results in the TD instability. The Lewis number (*Le*) of the mixture is the ratio of the thermal diffusivity to mass diffusivity. The TD instability is enhanced with mixtures of Lewis number below the critical value which is lower than 1 [51,52]. For 0.1 MPa, cellular instability was not present for 30 and 50 % H_2 as the Lewis number of these mixtures is within the stable regime ($0.8 < Le < 1.4$) [53]. As the hydrogen fraction increased to 70 %, flame front cellularity was shown at $\phi = 0.8$ ($Le < 0.8$), and at $\phi = 0.8$ and 1 for 100 % H_2. The hydrogen, which has a high mass diffusion coefficient, decreases *Le* and enhances the TD instability [54]. In contrast, flame instability has not been

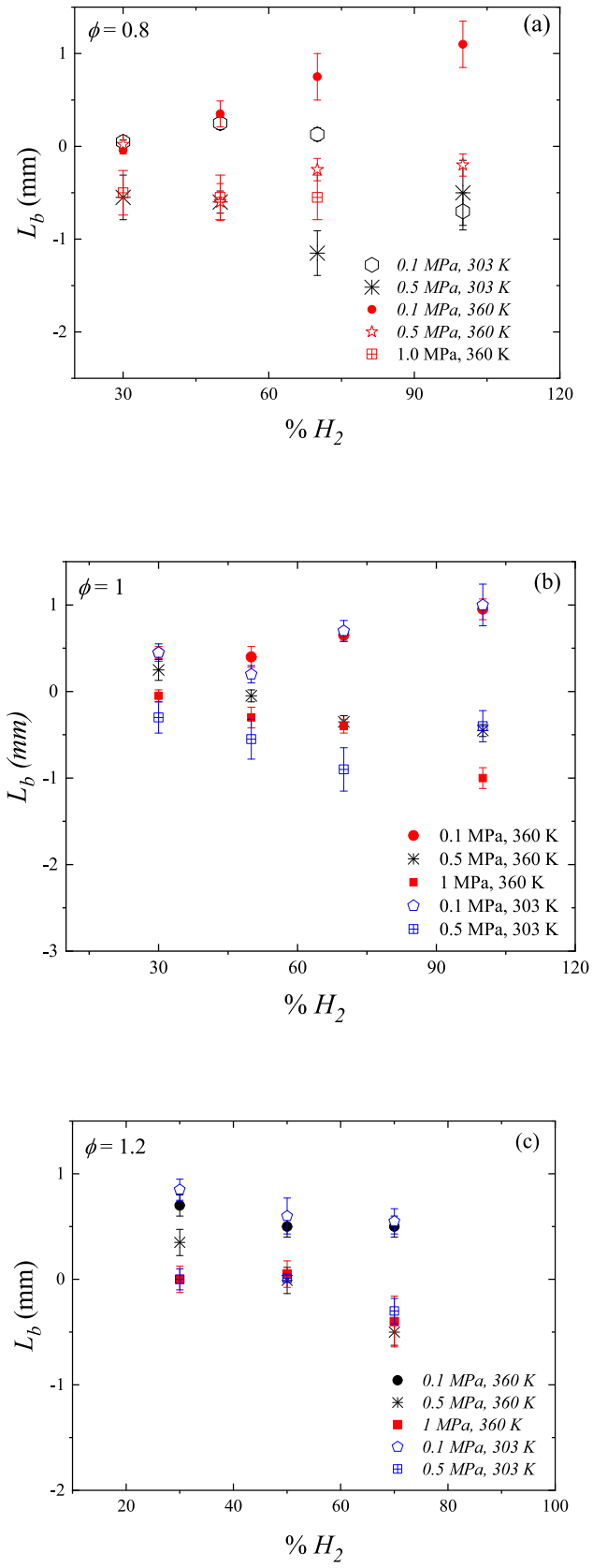

Fig. 12. Markstein length *vs.* hydrogen fraction for lean, stoichiometric and rich mixtures at different initial pressures and temperatures, (a) $\phi = 0.8$, (b) $\phi = 1$ and (c) $\phi = 1.2$.

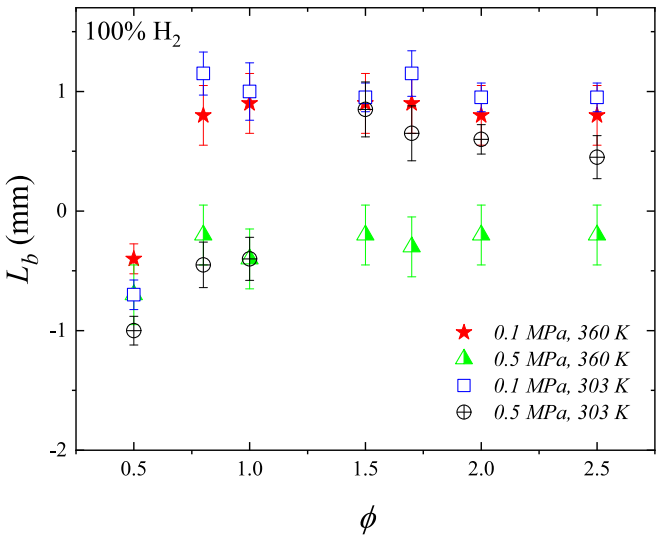

Fig. 13. The impact of pressure and temperature on the Markstein length at different equivalence ratios for pure hydrogen.

observed in the rich mixture of high H_2 concentrations within the field of view under initial pressure 0.1 MPa, as $Le > 1$.

For high pressure experiments (0.5 and 1 MPa), cellularity has been observed in all mixtures due to the DL and TD instabilities. The increased pressure promotes the DL instability, which is generated from the interaction of the flame with the hydrodynamic disturbances. The DL instability develops as the flame thickness decreases and/or the density ratio $\left(\frac{\rho_u}{\rho_b}\right)$ increases [19,45,51]. As the initial pressure increases, at a specific initial temperature, the change in density ratio is small while the decrease in the flame thickness is noticeable, resulting in hydrodynamic instability. As the initial temperature decreases, at a specific pressure, the density ratio increases while the change in flame thickness is small, advancing the onset of instability ($r_{cl} \propto T_u$). Thus, the DL instability is dominant in high pressure and low temperature flame propagations, due to the increased density ratio and decreased flame thickness.

The onset of cellularity, which is the transition point between the stable and unstable regimes, depends on thermal-diffusive and hydrodynamic effects. Increasing hydrogen fraction and pressure leads to the earlier onset of instability and a smaller critical flame radius. As the hydrogen fraction increases, Lewis number and flame thickness decrease, leading to the TD and DL instabilities. An example of this is presented in Fig. 4, which shows the critical flame radius for a stoichiometric mixture at 360 K. As the hydrogen fraction increases, the onset of instability appears earlier over the flame surface (reduced critical flame radius). For 0.5 MPa, 360 K and $\phi = 1$, r_{cl} is 26 mm for 30 % H_2, 13.2 mm for 50 % H_2, 10.5 mm for 70 % H_2 and 10 mm for pure H_2 fuel. r_{cl} also decreased with increasing pressure for all mixtures. r_{cl} for 30 % H_2 decreased from 26 mm at 0.5 MPa to 13 mm when the pressure increased to 1.0 MPa. So in summary, adding hydrogen, increasing pressure and reducing the temperature all promote the onset of cellularity.

3.2. Flame speeds and stretch rate

As the hydrogen fraction increases, the flame speed increases for all mixtures. As observed previously [7,16,17], hydrogen increases the flame temperature and supplies more active radicals to the reaction. In all mixtures considered here, the flame speed was high in the early stages of the flame propagation, due to the influence of the ignition energy [19,33]. The flame speed then decreases as the influence of the spark reduces [55]. Next, a fully developed laminar flame (stable region) is obtained until the onset of instability when the flame accelerates.

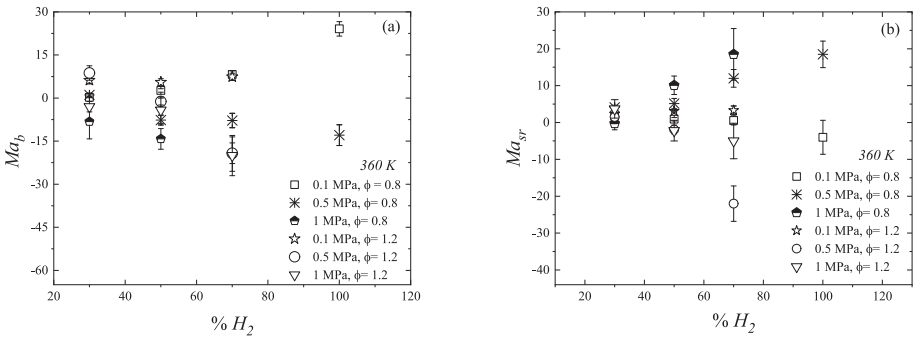

Fig. 14. Markstein number (Ma_b and Ma_{sr}) *vs.* hydrogen fraction at $\phi = 0.8$ and 1.2 and different initial pressures, (a) Ma_b and (b) Ma_{sr}.

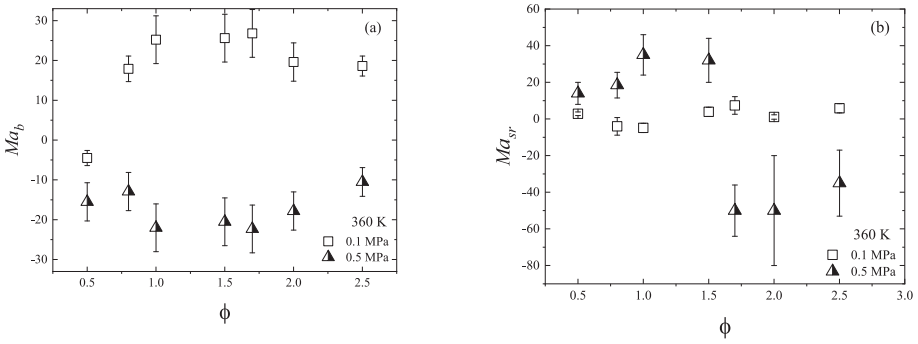

Fig. 15. Total (a) and strain rate (b) Markstein number *vs.* equivalence ratio for pure hydrogen at different initial pressures, (a) Ma_b and (b) Ma_{sr}.

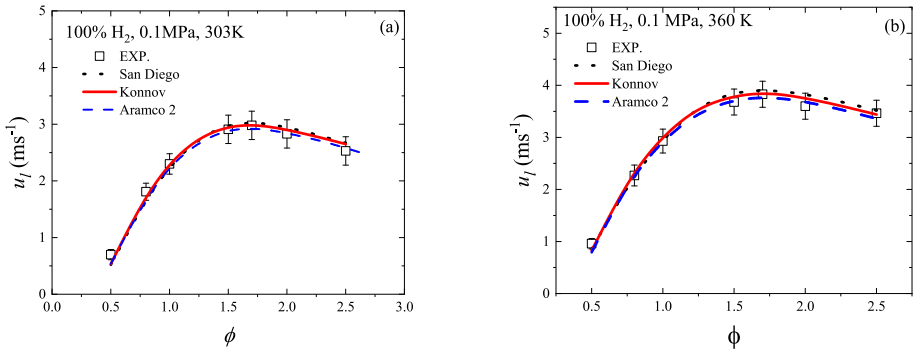

Fig. 16. Comparison between the experimentally derived laminar burning velocities for pure hydrogen with numerical predictions using different mechanisms at 0.1 MPa, (a) 303 K and (b) 360 K.

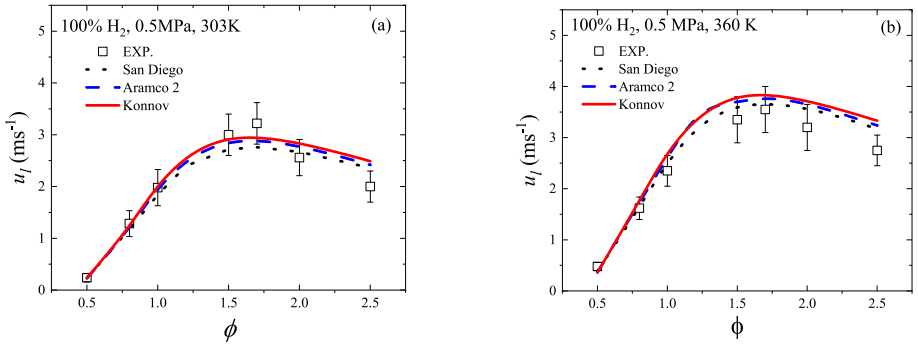

Fig. 17. Comparison between the experimentally derived laminar burning velocities for pure hydrogen with numerical predictions using different mechanisms at 0.5 MPa, (a) 303 K and (b) 360 K.

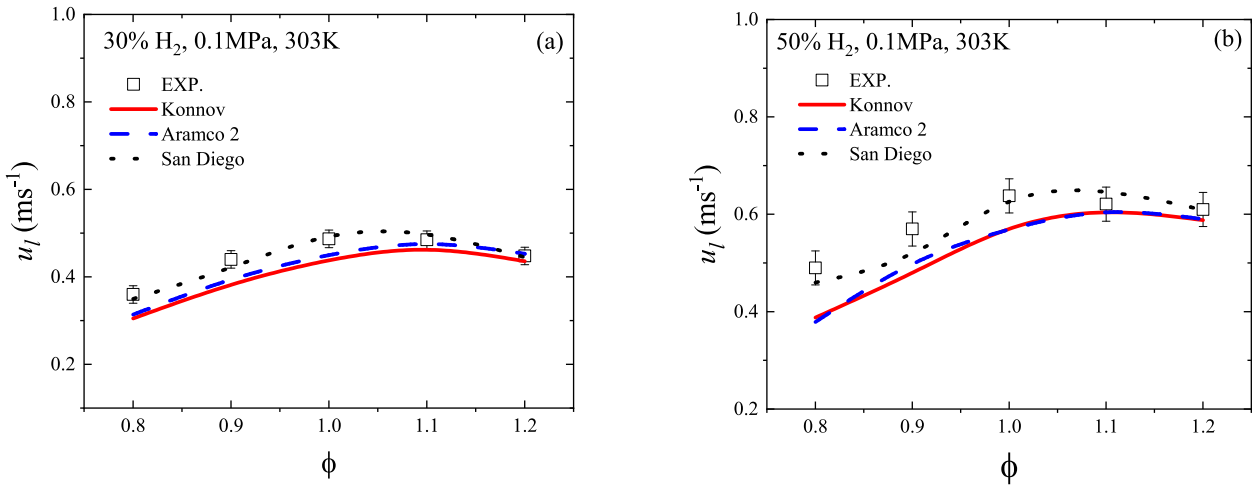

Fig. 18. Comparison between experimentally derived laminar burning velocities for methane/hydrogen mixtures with different mechanisms at 0.1 MPa and 303 K, (a) 30 % H_2 and (b) 50 % H_2.

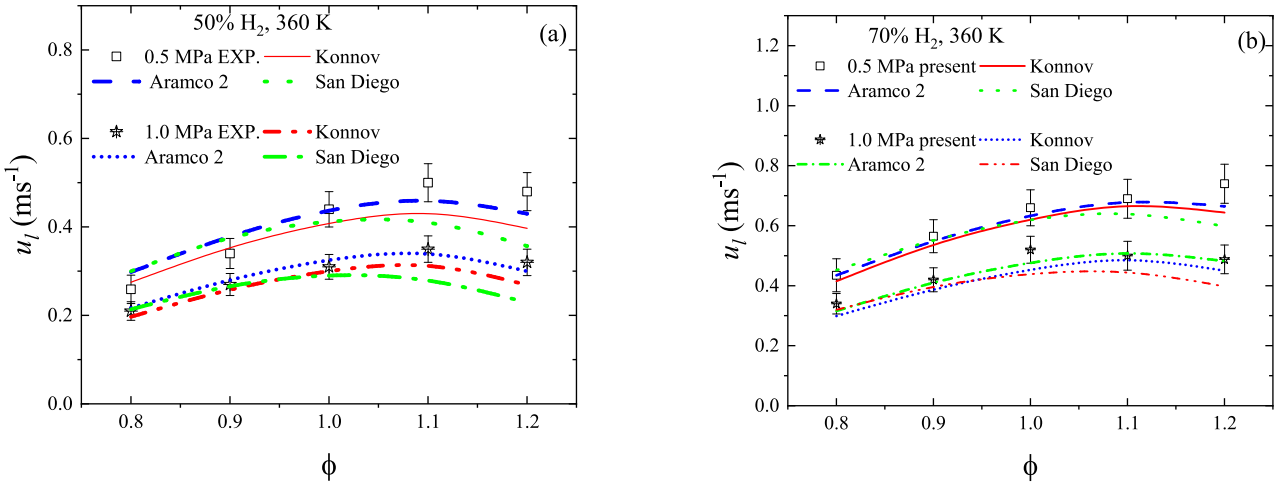

Fig. 19. Comparison between experimentally derived laminar burning velocities for methane/hydrogen mixtures with different mechanisms at 0.5, 1.0 MPa and 360 K, (a) 50 % H_2 and (b) 70 % H_2.

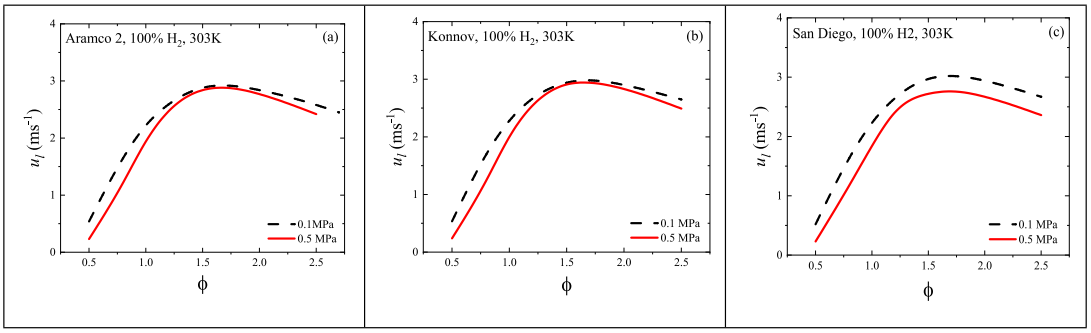

Fig. 20. Numerical predictions of laminar burning velocities *vs.* equivalence ratio for pure hydrogen at initial temperature of 303 K with initial pressure of 0.1 MPa and 0.5 MPa (a) Aramco 2.0 (b) Konnov and (c) San Diego.

In the high-pressure flame propagations with 30 % H_2, the flame speed in the stable region increased as the flame radius increased. However, for 70 % H_2 the flame speed decreases up to the critical flame radius after which it increases rapidly due to the increased flame surface area [37]. Neither trend was observed for pure hydrogen at 1.0 MPa. In this case, the flame speed increased with the flame radius from the early stages of flame propagation, due to the early development of the flame instability (Fig. 5b). Laminar burning velocity measurements in this case are not possible due to the absence of a stable region with laminar flame propagation. The slope of the flame speed as a function of flame radius for 1.0 MPa is higher than the cellularity-free flame propagation slope at 0.1 MPa (Fig. 5a). At high-pressure conditions, flame instabilities accelerate the pure hydrogen flames.

Fig. 6 shows the variation of flame speed with stretch rate at different

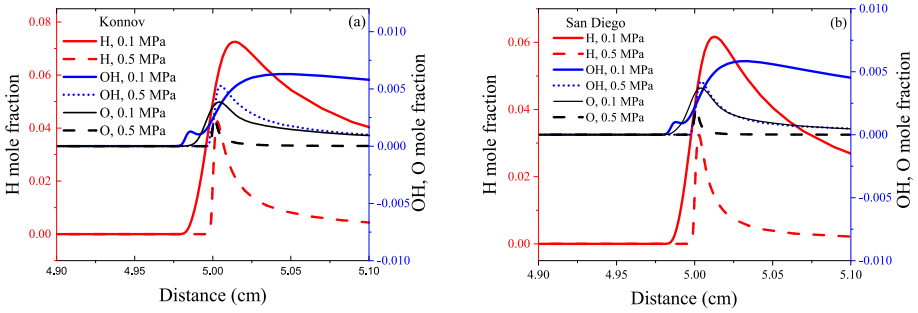

Fig. 21. Active radical concentrations for pure H_2 at 303 K and $\phi = 1.7$, from (a) Konnov and (b) San Diego mechanism.

pressures, H_2 fractions and equivalence ratios. The extrapolated data, Markstein length L_b and critical flame radius r_{cl} are also shown. For low pressure experiments (0.1 MPa), the flame propagated smoothly without flame cellularity within the field of view, and the value of S_n decreased with increasing stretch rate, indicating positive Markstein lengths in the rich mixture of 30 %, 50 % and 70 % H_2 mixtures (Fig. 6a–c). As the initial pressure increased, the gradient of the S_n-α curve decreased. For the stoichiometric mixture of 30 % H_2, L_b decreased from 0.4 mm at 0.1 MPa to 0.08 mm at 0.5 MPa and to −0.1 mm at 1.0 MPa. In the negative L_b cases, S_n increases as the stretch rate increases, lowering the un-stretched flame speed (S_s) and laminar burning velocity (u_l). This is the opposite of what happens for the positive L_b cases.

There are different sources of uncertainty in the derivation of laminar burning velocities from the measurements. Firstly, the uncertainty due to the linear extrapolation is tested using Eq. (2.10). The values of U_f vary between −0.05 and 0.15, indicating that linear extrapolation is valid and leads to uncertainties in the data presented here $< \pm 5$ % [12]. Thus, the linear extrapolation (Eq. (2.7)) is used to obtain the unstretched flame speed and Markstein length L_b. The second and most important source of uncertainty is due to the choice of the stable region (i.e. the choice of thresholds which define the end of the spark effect and the onset of instability). The stable region is very compact at high pressures and hydrogen fractions (Fig. 6d). In the present study, a minimum spark energy was used in all experiments, as the addition of hydrogen reduces the required ignition energy. The end of the spark energy effect was taken to be at a flame radius = 10 mm for 0.1 MPa [32] and 5 mm for higher pressure flame propagations [19]. Determining the onset of instability precisely is not straightforward. An example of the flame around the onset of instability is presented in Fig. 7 for 50 % H_2 with 0.5 MPa, 360 K and $\phi = 1$. The onset of instability could be associated with any of the 6 images.

The sensitivity of u_l to the selected point of instability is demonstrated in Fig. 8. Here, the number of points used for the extrapolation is varied to account for uncertainties in defining the boundary of the onset of instability as illustrated in Fig. 7. The uncertainty increased with the initial pressure and hydrogen fraction. The uncertainty in the laminar burning velocity increased from ±1.5 % of u_l for 30 % H_2 to ±3.5 % for 70 % H_2 and to ±12 % for pure H_2 at 0.5 MPa (Fig. 8a–c). As the initial pressure increased from 0.5 MPa to 1 MPa, the uncertainty increased from ±3.5 % of u_l to ±7.5 % with 70 % H_2. These uncertainties are included in the error bars of further results presented in this work. The uncertainty increased at high pressures and hydrogen concentrations due to the smaller number of points used in the extrapolation. For example, there was a shortage of data points for the cases with 100 % H_2, $\phi = 0.8$, 0.5 MPa and 360 K, as the spark effect vanished at a flame radius, $r = 5$ mm, and the onset of instability was determined to be between $r = 6$ and 7.5 mm.

3.3. Un-stretched laminar burning velocities

The stretched flame speed is extrapolated to zero stretch rate to obtain the un-stretched flame speed. The un-stretched flame speed is multiplied by the density ratio (Eq. (2.10)) to obtain the un-stretched laminar burning velocity (u_l). Fig. 9&10 show the variation of un-stretched laminar burning velocity with equivalence ratio for different H_2 fractions, pressures and temperatures. As the hydrogen fraction increases, the laminar burning velocity increases. The maximum laminar burning velocity occurs on the rich side of stoichiometric conditions. For example, for 30 % and 50 % H_2 it occurs at $\phi = 1.1$. However, it shifts to $\phi = 1.2$ for 70 % H_2 and to $\phi = 1.7$ for a pure H_2 flame.

This trend quantifies the effect of hydrogen volume fraction on laminar burning velocity. Hu et al. [11] have highlighted three regimes in H_2/CH_4 mixture flame propagation: (a) methane-dominated propagation for $H_2 < 60$ %, (b) a transition regime for 60 % $< H_2 <$ 80 % and (c) methane-inhibited hydrogen propagation where $H_2 > 80$ %. Therefore, the hydrogen fraction has the dominant effect on u_l.

In all experimental conditions for the methane-H_2 mixtures, the burning velocity decreased as the pressure increased for all equivalence ratios. This behaviour was the same for pure H_2 at 360 K. However, at the lower temperature (303 K), $\phi = 1.5$ and 1.7, higher u_l are measured at higher pressure, but the uncertainties are large and overlapping. (Fig. 10a). The laminar burning velocity would be expected to be lower at higher pressure, due to the increased effect of reaction $H + O_2 + M = HO_2 + M$ [56]. Therefore, this point has been considered for further analysis in the next section.

Fig. 11 compares the current results of the un-stretched laminar burning velocity with those from the literature at 0.1 MPa [11,14,57,58]. There is a good agreement between the present and previous results, with a maximum scatter of ± 13 % in the burning velocities for lean hydrogen flames. The issue of experimental scatter is well reported in the literature [47,59,60]. Such comparisons were not possible at high pressure, where the current work presents novel data that is not present in the literature. However, the good agreement found for overlapping conditions provides an indication of the robustness of the current study.

3.4. Markstein number and Markstein length

The Markstein number is used to quantify the effect of flame stretch rate on the flame speed, and hence on the un-stretched laminar burning velocity [33,50]. The effect of stretch rate on flame speed depends on the Zel′dovich number, *Ze*, and the Lewis number, *Le* [7]. The Markstein length (L_b) is a function of the physical and chemical properties of the mixture (*Le* and *Ze*). As the hydrogen fraction increases, non-dimensional activation energy (Zel′dovich number, *Ze*) decreases due to the increased adiabatic flame temperature and *Le* decreases due to the hydrogen diffusivity [7]. Moreover, previous research on premixed pure H_2 and pure CH_4 [9,33] determined L_b in terms of the Lewis number ($L_b = -0.059$ mm with $Le = 0.3$ for pure H_2, and $L_b = 0.74$ mm with $Le = 0.9$ for pure CH_4).

Fig. 12&13 show the effects of hydrogen, pressure and temperature on L_b for different mixtures. For lean and stoichiometric mixtures at 0.1 MPa, L_b increases with H_2 fraction (Fig. 12a&b). However, L_b decreases with H_2 fraction for lean and stoichiometric mixtures at higher initial

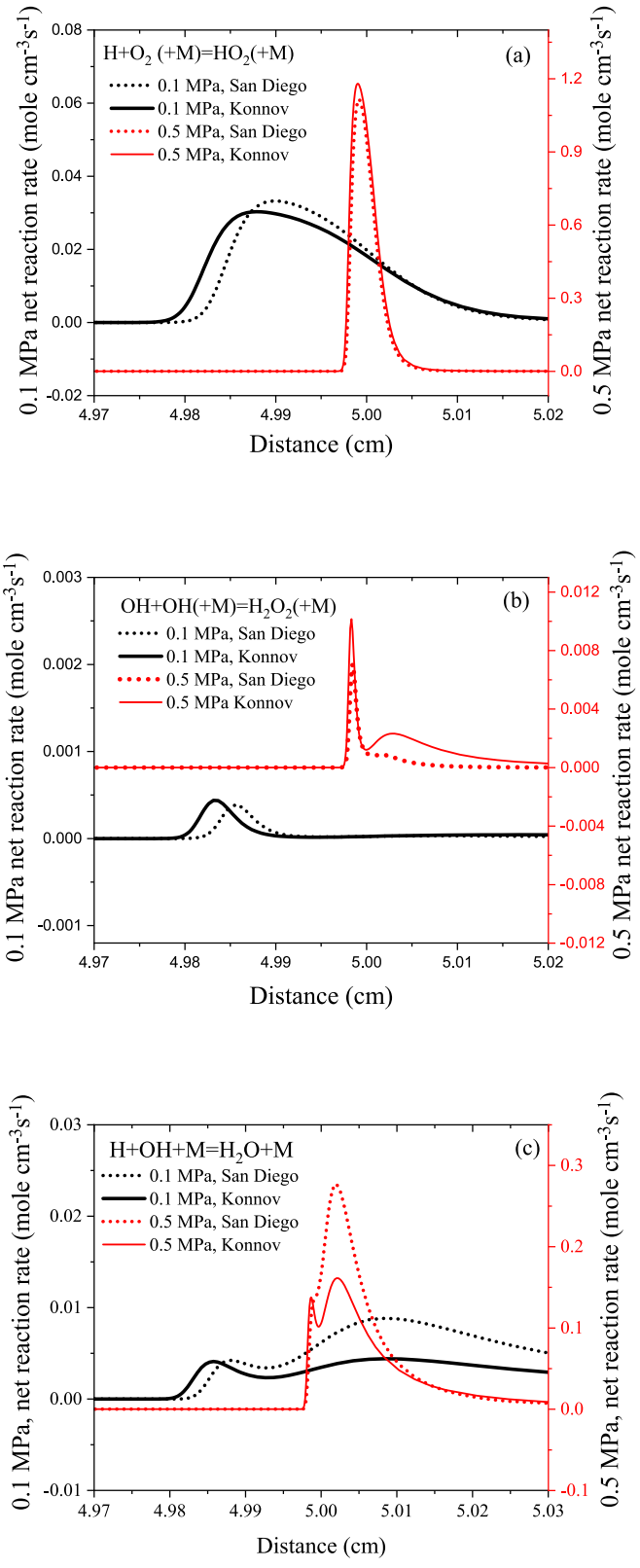

Fig. 22. Net rate of key pressure dependent reactions for pure H_2/air mixtures at 303 K and ϕ = 1.7, from simulations using the San Diego and Konnov reaction mechanisms (a) H + O_2 (+M) = HO_2 (+M), (b) OH + OH(+M) = H_2O_2(+M) and (c) H + OH + M = H_2O + M.

pressures. As the pressure increases, L_b decreases except for rich mixtures with 50 and 70 % H_2 fraction (Fig. 12c) where L_b increases slightly when the pressure increases from 0.5 to 1.0 MPa. As the temperature is increased from 303 to 360 K at 0.5 MPa, L_b increases significantly in the lean and stoichiometric mixtures (Fig. 12a&b) but decreases slightly in the rich mixtures (Fig. 12c). The data for pure hydrogen at 1 MPa is not presented here due to the early onset of flame cellularity. Comparing with previous results [33] for pure CH_4 flame at 0.1, 0.5, and 1.0 MPa, the present L_b is lower than for the pure CH_4 results. This is expected as L_b for H_2 is lower than that of CH_4, which means adding hydrogen to methane lowers L_b.

Markstein length is normalized by the flame thickness to obtain the Markstein number (Ma_b). The strain rate Markstein number Ma_{sr} was calculated using the method described in [44]. Fig. 14&15 show how Ma_b and Ma_{sr} vary with H_2 fraction for a range of equivalence ratios, pressures and temperatures. Ma_b decreases with pressure and hydrogen fraction in the lean and rich mixtures (Fig. 14a), except for the case with $\phi = 0.8$ at 0.1 MPa where the Ma_b increases with increased H_2 fraction. In the lean mixture, Ma_{sr} increases as pressure increases. However, as H_2 fraction increases Ma_{sr} varies non-monotonically for lean and rich cases (Fig. 14b).

Fig. 15 presents Ma_b and Ma_{sr} for pure H_2 at 0.1 and 0.5 MPa as a function of equivalence ratio. It can be seen that Ma_b decreases with pressure. For 0.1 MPa, Ma_b increases as the mixture changes from lean to rich and eventually decreases for $\phi \geq 2$. The maximum Ma_b was at $\phi = 1.7$ which corresponds to the minimum flame thickness and maximum u_l. However, at 0.5 MPa Ma_b decreases as the mixture changes from a lean to a rich mixture achieving its minimum value at $\phi = 1.7$, increasing thereafter. Ma_{sr} increases with pressure for $\phi \leq 1.5$, while it decreases with pressure for $\phi > 1.5$ (Fig. 15b).

As presented in Fig. 8, the uncertainty in the derived values of L_b, Ma_b and Ma_{sr} is large in the high pressure cases with high H_2 volume fractions, and this was also reported in [26]. For example, Ma_{sr} and Ma_b for the cases with $\phi = 0.8$, 70 % H_2 at 1 MPa and $\phi = 2$, 100 % H_2 at 0.5 MPa have large error bars which vary from 30 to 60 % of the nominal value (Fig. 14&15). On the other hand, the error bar is small in the cases with 30 and 50 % H_2 at 0.1 MPa (≤20 % of the nominal value). The large uncertainty is due to the small number of points used for the extrapolation (stable regime), as discussed with respect to Fig. 8. At 1 MPa with $\phi = 0.8$ and 70 % H_2, the stable regime was between flame radius, $r = 5$ mm to $r = 7.5 \pm 1$ mm, while it was in the range of 10–65 mm at 0.1 MPa with $\phi = 1$ and 30 % H_2. The uncertainty in the high pressure and high H_2 cases is affected from both sides (spark effects and the onset of instability) due to the minimal number of points used in the extrapolation. All the experimental data reported in this study are presented in **Appendix A**.

4. Comparisons between the experimental and simulated laminar burning velocities for methane/hydrogen oxidation

An important reason for measuring the un-stretched laminar burning velocity is to provide reliable data for validating kinetics models used in the optimal design of gas turbine combustors and other practical applications. However, there is uncertainty in both the experimental measurements (as discussed above) and numerical predictions [30]. For the comparisons reported here, the premixed laminar burning velocity was calculated using the one dimensional steady freely propagating planar flame code, Chemkin-Pro 21 [61]. In this code, the 1D planar flame is modelled by solving the governing continuity, energy and species conservation equations using detailed chemical kinetics. Thermal diffusion (the Soret effect) and a multi-component diffusion model were used to evaluate the transport properties. Further details on the premixed laminar burning velocity calculations are available in [61].

Three H_2/CH_4 mechanisms were compared with the experimentally derived laminar burning velocities presented above. These are: (i) the latest version of the San Diego mechanism which has 58 species and 270

Table A1
Measured laminar burning velocity, Markstein length, critical flame radius flame thickness stretch and strain Markstein number for 30 % hydrogen fraction.

Experimental Conditions	ϕ	u_l(m/s)	L_b (mm)	r_{cl} (mm)	δ_l(mm)	Ma_b	Ma_{sr}
$0.1 \pm 25 \times 10^{-4}$ MPa, 303 ± 2 K	0.8	0.36 ± 0.012	0.055 ± 0.006		0.156	0.35 ± 0.06	1.55 ± 0.18
	0.9	0.44 ± 0.024	0.25 ± 0.006		0.135	1.8 ± 0.6	1.63 ± 0.12
	1.0	0.487 ± 0.024	0.45 ± 0.006		0.118	3.8 ± 0.7	1.85 ± 0.18
	1.1	0.485 ± 0.024	0.6 ± 0.006		0.119	5 ± 0.06	2.1 ± 0.18
	1.2	0.448 ± 0.024	0.85 ± 0.006		0.130	6.5 ± 0.5	2.37 ± 0.12
$0.1 \pm 25 \times 10^{-4}$ MPa, 360 ± 2 K	0.8	0.43 ± 0.024	0.04 ± 0.012		0.156	0.25 ± 0.06	1.75 ± 0.12
	0.9	0.575 ± 0.024	0.4 ± 0.012		0.118	3.4 ± 0.8	2.37 ± 0.12
	1.0	0.63 ± 0.024	0.45 ± 0.012		0.108	4.1 ± 0.6	2.42 ± 0.12
	1.1	0.625 ± 0.024	0.5 ± 0.012		0.110	4.5 ± 1.2	2.5 ± 0.24
	1.2	0.62 ± 0.024	0.7 ± 0.012		0.111	6.2 ± 0.12	2.38 ± 0.12
$0.5 \pm 25 \times 10^{-4}$ MPa, 303 ± 2 K	0.8	0.14 ± 0.024	−0.55 ± 0.24	15.5 ± 1.2	0.0889	−6.1 ± 1.8	1.5 ± 1.8
	0.9	0.2 ± 0.024	−0.35 ± 0.12	17.5 ± 1.2	0.0605	−5.8 ± 1	1.8 ± 0.6
	1.0	0.25 ± 0.024	−0.3 ± 0.06	18.5 ± 1.2	0.0498	−6 ± 0.6	1.1 ± 1.8
	1.1	0.256 ± 0.024	−0.2 ± 0.06	26 ± 1.2	0.0493	−4 ± 0.6	0.9 ± 0.36
	1.2	0.23 ± 0.024	−0.55 ± 0.08	33 ± 1.2	0.055	−3.9 ± 0.6	0.8 ± 0.18
$0.5 \pm 25 \times 10^{-4}$ MPa, 360 ± 2 K	0.8	0.24 ± 0.024	0.07 ± 0.024	24 ± 1.2	0.0616	1.1 ± 1	4.1 ± 0.6
	0.9	0.27 ± 0.024	0.02 ± 0.024	26 ± 1.2	0.0548	0.36 ± 0.24	−4 ± 1.2
	1.0	0.34 ± 0.024	0.2 ± 0.18	26 ± 1.2	0.0429	6.3 ± 3.6	1.3 ± 2
	1.1	0.38 ± 0.024	0.25 ± 0.12	29.5 ± 1.2	0.0395	6.25 ± 2.4	−2 ± 2
	1.2	0.38 ± 0.024	0.35 ± 0.12	37.7 ± 1.2	0.0395	8.75 ± 3	1.5 ± 1.8
$1.0 \pm 25 \times 10^{-4}$ MPa, 360 ± 2 K	0.8	0.13 ± 0.018	−0.5 ± 0.24	11 ± 1.2	0.0594	−8.2 ± 4.8	−0.25 ± 1.2
	0.9	0.2 ± 0.018	−0.1 ± 0.06	13 ± 1.2	0.0373	−2.6 ± 0.6	−1.1 ± 0.63
	1.0	0.26 ± 0.018	−0.05 ± 0.06	15.5 ± 1.2	0.03	−2.5 ± 1	−3.8 ± 2
	1.1	0.27 ± 0.018	−0.1 ± 0.11	16.5 ± 1.2	0.0287	−5 ± 2.4	6.25 ± 3.6
	1.2	0.25 ± 0.018	0.01 ± 0.09	25 ± 1.2	0.0316	−3 ± 2.4	3.7 ± 1.7

Table A2
Measured laminar burning velocity, Markstein length, critical flame radius flame thickness stretch and strain Markstein number for 50 % hydrogen fraction.

Experimental Conditions	ϕ	u_l(m/s)	L_b (mm)	r_{cl} (mm)	δ_l(mm)	Ma_b	Ma_{sr}
$0.1 \pm 25 \times 10^{-4}$ MPa, 303 ± 2 K	0.8	0.51 ± 0.036	0.25 ± 0.06		0.12	2 ± 0.6	1.45 ± 0.6
	0.9	0.57 ± 0.036	0.4 ± 0.02		0.109	3.6 ± 0.12	1.44 ± 0.12
	1.0	0.63 ± 0.036	0.2 ± 0.02		0.1	2 ± 0.24	1.85 ± 0.24
	1.1	0.62 ± 0.036	0.4 ± 0.12		0.103	3.8 ± 1.2	1.9 ± 0.36
	1.2	0.61 ± 0.036	0.6 ± 0.12		0.106	5.6 ± 1.2	2.15 ± 0.18
$0.1 \pm 25 \times 10^{-4}$ MPa, 360 ± 2 K	0.8	0.57 ± 0.036	0.35 ± 0.06		0.13	2.65 ± 0.6	0.9 ± 0.36
	0.9	0.71 ± 0.036	0.2 ± 0.04		0.105	1.89 ± 0.6	1.4 ± 0.6
	1.0	0.84 ± 0.048	0.4 ± 0.12		0.09	5.4 ± 1.5	2.7 ± 0.7
	1.1	0.86 ± 0.036	0.5 ± 0.12		0.089	5.5 ± 1.5	2.95 ± 0.48
	1.2	0.85 ± 0.036	0.5 ± 0.04		0.091	5.48 ± 0.12	3.1 ± 0.6
$0.5 \pm 25 \times 10^{-4}$ MPa, 303 ± 2 K	0.8	0.21 ± 0.036	−0.6 ± 0.24	11.5 ± 1.2	0.075	−7.79 ± 2.4	3.05 ± 0.8
	0.9	0.26 ± 0.036	−0.7 ± 0.24	12.2 ± 1.2	0.05	−13.8 ± 2.4	5.1 ± 1.2
	1.0	0.30 ± 0.036	−0.55 ± 0.24	13.4 ± 1.2	0.045	−12.1 ± 2.4	1.35 ± 0.8
	1.1	0.32 ± 0.036	−0.3 ± 0.18	17.3 ± 1.2	0.043	−6.9 ± 2.4	2.1 ± 0.9
	1.2	0.3 ± 0.036	0.03 ± 0.024	39 ± 1.2	0.047	0.62 ± 2.4	3.15 ± 0.6
$0.5 \pm 25 \times 10^{-4}$ MPa, 360 ± 2 K	0.8	0.24 ± 0.036	−0.6 ± 0.12	12 ± 1.2	0.078	−7.65 ± 1.2	5.15 ± 1.2
	0.9	0.34 ± 0.036	−0.15 ± 0.09	13.2 ± 1.2	0.047	−3.1 ± 1.8	13.73 ± 3.6
	1.0	0.44 ± 0.036	−0.09 ± 0.06	15 ± 1.2	0.037	−2.4 ± 1.2	8.73 ± 3
	1.1	0.5 ± 0.036	−0.06 ± 0.06	18 ± 1.2	0.033	−1.9 ± 1.8	−0.8 ± 0.8
	1.2	0.48 ± 0.036	−0.075 ± 0.04	25 ± 1.2	0.035	−1.2 ± 1.2	−1.9 ± 0.7
$1.0 \pm 25 \times 10^{-4}$ MPa, 360 ± 2 K	0.8	0.22 ± 0.036	−0.55 ± 0.12	8 ± 1.2	0.038	−14.2 ± 2.4	10.1 ± 2.4
	0.9	0.27 ± 0.036	−0.45 ± 0.24	9.8 ± 1.2	0.031	−13.4 ± 4.8	11 ± 4.8
	1.0	0.31 ± 0.036	−0.3 ± 0.18	11.2 ± 1.2	0.027	−10.2 ± 4.8	12 ± 8
	1.1	0.35 ± 0.036	−0.25 ± 0.1.2	13.3 ± 1.2	0.025	−10.1 ± 3.6	1 ± 3.6
	1.2	0.32 ± 0.036	−0.1 ± 0.08	21.5 ± 1.2	0.027	−4.2 ± 4.8	−2.2 ± 1.8

elementary reactions [34,35]; (ii) the Konnov reduced mechanism with 27 species and 177 elementary reactions [30,36] and (iii) the Aramco 2 reduced mechanism with 25 species and 105 elementary reactions [36]. These mechanisms were selected as they were previously validated using low pressure experimental data [30,35,36] and cover a range of mechanism sizes with respect to numbers of species, the lowest having 25 species and the highest 58.

A comparison of predicted and experimentally derived laminar burning velocities for pure H_2-air and H_2–CH_4–air mixtures at 0.1, 0.5 and 1 MPa is presented in Figs. 16-19. All of the numerical predictions for low-pressure flame agree well with the experimentally derived laminar burning velocities. However, there is worse agreement for rich mixture flames, particularly as the pressure increases (Fig. 17&19), although the numerical predictions remain within the uncertainty of the experimental measurements. For pure hydrogen at $\phi = 2.5$, all of the mechanisms produced higher laminar burning velocities than the experiments. Both the Aramco2.0 and Konnov mechanisms give similar predictions across all conditions (Fig. 16&17). The San Diego mechanism predicts higher H_2/CH_4 burning velocities compared to the other two schemes (Fig. 18). At higher pressures there is a larger deviation between the predicted burning velocities from the three schemes and for these conditions, the Aramco scheme simulates higher laminar burning velocities (Fig. 19a). The C1–C2 chemistry is now playing a role and the Aramco and Konnov schemes use the PLOG formulation for a number of pressure dependent reactions within the C1–C2 scheme, whereas the San Diego mechanism uses Troe fall-off. There are clear differences in the parameterization of key pressure dependent reactions between the schemes.

Table A3
Measured laminar burning velocity, Markstein length, critical flame radius flame thickness stretch and strain Markstein number for 70 % hydrogen fraction.

Experimental Conditions	ϕ	u_l(m/s)	L_b (mm)	r_{cl} (mm)	δ_l(mm)	Ma_b	Ma_{sr}
$0.1 \pm 25 \times 10^{-4}$ MPa, 303 ± 2 K	0.8	0.71 ± 0.06	0.1 ± 0.06	35 ± 1.2	0.097	1.25 ± 1.2	1.2 ± 0.36
	0.9	0.84 ± 0.06	0.35 ± 0.06	40 ± 1.2	0.085	4.1 ± 1	1.7 ± 0.3
	1.0	0.95 ± 0.048	0.7 ± 0.0	–	0.076	9.1 ± 0.00	1.55 ± 0.6
	1.1	0.99 ± 0.042	0.5 ± 0.0	–	0.075	6.62 ± 0.06	2.1 ± 0.6
	1.2	0.99 ± 0.048	0.55 ± 0.06	–	0.077	6.1 ± 0.48	1.7 ± 0.42
$0.1 \pm 25 \times 10^{-4}$ MPa, 360 ± 2 K	0.8	0.92 ± 0.06	0.75 ± 0.08	46 ± 1.2	0.091	8.2 ± 1.2	0.55 ± 0.6
	0.9	1.06 ± 0.06	0.65 ± 0.1	53 ± 1.2	0.08	8 ± 1.2	1.34 ± 1.8
	1.0	1.28 ± 0.07	0.65 ± 0.12		0.067	9.65 ± 1.8	1.2 ± 0.6
	1.1	1.34 ± 0.052	0.6 ± 0.06		0.067	9 ± 1.2	2.2 ± 1
	1.2	1.35 ± 0.048	0.5 ± 0.12		0.067	7.4 ± 0.6	3.3 ± 1
$0.5 \pm 25 \times 10^{-4}$ MPa, 303 ± 2 K	0.8	0.29 ± 0.048	−1.15 ± 0.3	8.2 ± 0.6	0.052	–22 ± 4.8	1.05 ± 0.6
	0.9	0.37 ± 0.048	−0.8 ± 0.18	10 ± 0.6	0.042	−19.2 ± 2.4	1.75 ± 1.2
	1.0	0.44 ± 0.048	−0.9 ± 0.36	11.7 ± 0.6	0.035	−24.5 ± 8	3 ± 6
	1.1	0.51 ± 0.048	−0.35 ± 0.3	13.8 ± 0.6	0.031	−12 ± 4.8	−1.2 ± 1.8
	1.2	0.49 ± 0.048	−0.3 ± 0.3	14.5 ± 0.6	0.033	−9 ± 4.8	−0.2 ± 0.36
$0.5 \pm 25 \times 10^{-4}$ MPa, 360 ± 2 K	0.8	0.43 ± 0.06	−0.25 ± 0.24	9.1 ± 0.6	0.042	−5.8 ± 4.8	12 ± 2.4
	0.9	0.56 ± 0.06	−0.25 ± 0.12	10.5 ± 0.6	0.032	−7.6 ± 3.6	31 ± 11
	1.0	0.66 ± 0.06	−0.35 ± 0.18	11 ± 0.6	0.028	−12.3 ± 4.8	35 ± 11
	1.1	0.69 ± 0.055	−0.55 ± 0.24	12.4 ± 0.6	0.027	−20 ± 3.6	−7 ± 8.5
	1.2	0.74 ± 0.055	−0.5 ± 0.12	13 ± 0.6	0.026	−19.2 ± 3.6	–22 ± 4.8
$1.0 \pm 25 \times 10^{-4}$ MPa, 360 ± 2 K	0.8	0.34 ± 0.048	−0.55 ± 0.18	7.5 ± 0.6	0.028	−19.5 ± 3	18.5 ± 5
	0.9	0.42 ± 0.048	−0.75 ± 0.24	9 ± 0.6	0.023	–33 ± 4.8	30 ± 6
	1.0	0.52 ± 0.048	−0.4 ± 0.12	9.5 ± 0.6	0.019	−21 ± 4.8	30 ± 8
	1.1	0.5 ± 0.058	−0.6 ± 0.12	10.6 ± 0.6	0.02	−28 ± 4.8	28 ± 7
	1.2	0.49 ± 0.06	−0.4 ± 0.12	11.9 ± 0.6	0.025	−20 ± 4.8	−3 ± 6

Table A4
Measured laminar burning velocity, Markstein length, critical flame radius flame thickness stretch and strain Markstein number for pure hydrogen explosions.

Experimental Conditions	ϕ	u_l(m/s)	L_b (mm)	r_{cl} (mm)	δ_l(mm)	Ma_b	Ma_{sr}
$0.1 \pm 25 \times 10^{-4}$ MPa, 303 ± 2 K	0.5	0.7 ± 0.06	−0.7 ± 0.24	18 ± 1.2	0.103	−6.7 ± 0.6	12.3 ± 2.4
	0.8	1.79 ± 0.12	1.15 ± 0.3	36 ± 1.2	0.047	24.1 ± 2.5	−1.1 ± 1.2
	1.0	2.3 ± 0.12	1.0 ± 0.3	45.5 ± 1.2	0.04	25 ± 4.8	0.44 ± 0.48
	1.5	2.91 ± 0.06	0.95 ± 0.18	–	0.037	25.2 ± 3.6	6.2 ± 1.2
	1.7	2.98 ± 0.06	1.15 ± 0.18	–	0.038	30 ± 2.4	9.85 ± 2.4
	2	2.83 ± 0.07	0.95 ± 0.18	–	0.043	22 ± 3.6	4.6 ± 1.2
	2.5	2.53 ± 0.06	0.95 ± 0.18	–	0.052	18 ± 1.2	3.8 ± 1.2
$0.1 \pm 25 \times 10^{-4}$ MPa, 360 ± 2 K	0.5	0.98 ± 0.07	−0.3 ± 0.18	19.4 ± 1.2	0.087	−4.5 ± 2.4	2.85 ± 1.2
	0.8	2.27 ± 0.08	0.8 ± 0.18	41.8 ± 1.2	0.044	17.9 ± 3.6	−4 ± 4.8
	1.0	2.93 ± 0.12	0.95 ± 0.3	57 ± 1.2	0.037	25.2 ± 6	−4.87 ± 1.8
	1.5	3.68 ± 0.08	0.9 ± 0.06	–	0.035	25.6 ± 1.2	3.9 ± 2.4
	1.7	3.83 ± 0.06	0.95 ± 0.12	–	0.035	26.8 ± 2.4	7.4 ± 4.9
	2	3.55 ± 0.06	0.8 ± 0.12	–	0.04	19.6 ± 1.2	1.1 ± 1.2
	2.5	3.46 ± 0.06	0.85 ± 0.18	–	0.045	18.6 ± 2.4	5.85 ± 1.2
$0.5 \pm 25 \times 10^{-4}$ MPa, 303 ± 2 K	0.5	0.24 ± 0.12	−1 ± 0.6	6.2 ± 0.6	0.0166	−2.7 ± 1.2	2.7 ± 1.2
	0.8	1.28 ± 0.15	−0.45 ± 0.6	7 ± 0.6	0.100	−3.95 ± 2.4	2.1 ± 1.2
	1.0	1.98 ± 0.24	−0.4 ± 0.6	11 ± 0.6	0.169	−5 ± 2.4	3.5 ± 3
	1.5	3 ± 0.36	0.85 ± 0.18	16 ± 0.6	0.307	13.4 ± 3.6	3.65 ± 2.4
	1.7	3.22 ± 0.36	0.65 ± 0.6	17.5 ± 0.6	0.349	11.5 ± 4.8	−1 ± 3.6
	2	2.56 ± 0.36	0.6 ± 0.36	21.4 ± 0.6	0.286	7.2 ± 2.4	0.17 ± 0.18
	2.5	2 ± 0.3	0.45 ± 0.48	30 ± 0.6	0.244	3.8 ± 3.6	0.6 ± 2.4
$0.5 \pm 25 \times 10^{-4}$ MPa, 360 ± 2 K	0.5	0.48 ± 0.36	−0.7 ± 0.48	6.3 ± 0.6	0.045	−15.5 ± 2.4	14 ± 4.8
	0.8	1.62 ± 0.2	−0.2 ± 0.24	6.6 ± 0.6	0.015	−12.9 ± 2.4	18.5 ± 4.8
	1.0	2.35 ± 0.3	−0.45 ± 0.36	10 ± 1.8	0.011	–22.7 ± 4.8	35 ± 12
	1.5	3.35 ± 0.4	−0.2 ± 0.18	13 ± 1.8	0.0097	−20.5 ± 4	32 ± 14
	1.7	3.55 ± 0.42	−0.3 ± 0.24	14 ± 0.6	0.0096	−25.3 ± 6	−50 ± 29
	2	3.2 ± 0.36	−0.2 ± 0.18	14.5 ± 0.6	0.0111	−17.8 ± 3.6	−50 ± 29
	2.5	2.75 ± 0.36	−0.15 ± 0.12	17.5 ± 0.6	0.014	−10.5 ± 4.8	−35 ± 19

Another difference between the predicted laminar burning velocities is observed for pure hydrogen at high pressure and low temperature. As shown in Fig. 10, the laminar burning velocities at equivalence ratios of 1.5 and 1.7 for 303 K did not decrease as the pressure increased from 0.1 to 0.5 MPa and the measurement uncertainties overlapped. This trend is reasonably well matched by predictions based on the Aramaco2.0 and Konnov kinetics which show convergence of the predicted u_l at $\phi = 1.5$ (Fig. 20). However, the predicted u_l using the San Diego mechanism decreases as the pressure increases over all values of ϕ. To clarify the prediction of u_l with the pressure rise, selected species concentrations and net rates of reaction based on the simulations are presented. Previous reaction analysis on methane/hydrogen mixtures [11,35] showed that as the initial pressure increased, the mole fractions of the three active radicals (H, O, OH) declined significantly, lowering the laminar burning velocity. The Konnov and San Diego mechanisms are used to present the mole fraction of these active species for a small interval of 0.1–0.2 mm in which the main chemical reactions take place (Fig. 21). The Konnov mechanism showed that as the pressure increases from 0.1 to 0.5 MPa, the peak mole fractions of H, O and OH reduce by 42, 50 and 8 %, respectively. However, the reductions in these species mole fractions are 48 %, 57 % and 26 % when using the San Diego scheme. The minimum reduction of the three active species can explain

the experimental finding at Fig. 10a. It is clear that as the pressure increases, the reduction in active radical concentrations is larger for San Diego mechanism than for the Konnov scheme, which could explain the differences between the laminar burning velocities predicted from two schemes.

In order to investigate the reasons for these differences further, the net rates of selected pressure dependent reactions are presented in Fig. 22. The difference between the two schemes for the rate of the main chain branching reaction $H + O_2 = OH + O$ is very small at both pressures and thus is not shown. The description of the competing termination reaction $H + O_2 (+M) = HO_2 (+M)$ varies between the schemes. Each scheme uses a Troe fall-off formulation but the parameterization of the low pressure limit Arrhenius expressions and collider efficiencies for species such as H_2O and H_2 differ. However, this leads to only small differences in the peak rate of reactions $H + O_2 (+M) = HO_2 (+M)$, $OH + OH (+M) = H_2O_2 (+M)$ between the two schemes for the H_2 air flame at 303 K and $\phi = 1.7$ (Fig. 22a). There are also slight differences in the net rate of reaction $OH + OH (+M) = H_2O_2 (+M)$ between the two schemes as presented in Fig. 22b. The reaction is described in the form $H_2O_2 (+M) = OH + OH (+M)$, using the same low and high pressure limits and collider efficiencies in the Aramco and Konnov schemes although a small difference exists in the Troe parameters. The San Diego mechanism expresses this reaction in its reverse form $OH + OH (+M) = H_2O_2 (+M)$ but again this does not lead to large discrepancies in the net reaction rate. There are however quite large discrepancies in the net rate of the radical recombination reaction $H + OH + M = H_2O + M$ between the Konnov and San Diego schemes (Fig. 22c) which will impact on the concentration of the active radial pool. These are particularly pronounced for the high pressure conditions and could explain the lower radical concentrations predicted using the San Diego scheme at higher pressures, which in turn lead to lower predicted flame speeds.

5. Conclusions

Flame speeds, un-stretched laminar burning velocities and Markstein numbers for H_2 and H_2/CH_4/air mixtures were derived from experimental measurements at elevated pressure by employing a spherically expanding flame propagation technique. The following conclusions can be drawn:

1- Laminar burning velocities increase with both the H_2 fraction in the mixture and with temperature. As the pressure increased, the laminar burning velocity decreased except for the cases of pure hydrogen/air mixtures and low-temperature flames at $\phi = 1.5$ and 1.7 where the burning velocity is unaffected by pressure. The latter is due to the low reduction of H and OH mole fractions in such cases.
2- For high pressure experiments (0.5 and 1 MPa), cellularity has been observed in all mixtures due to DL and TD instabilities. Cellularity is observed more quickly for larger hydrogen fractions and pressures and for lower temperatures.
3- Ma_{sr} varies non-monotonically with the pressure and hydrogen fractions due to the competing effects of the Zel′dovich, *Ze*, and Lewis numbers, *Le*.
4- For pure H_2 flames, Ma_{sr} increases with pressure for $\phi \leq 1.5$, and decreases with pressure for $\phi > 1.5$ due to the increased value of *Le* in the rich H_2/air mixture.
5- Uncertainties for the values of u_l, L_b, Ma_b and Ma_{sr} caused by extrapolation increase with increasing pressure and H_2 volumetric fraction due to the lower number of experimental points that are available for use within the extrapolation.
6- The experimentally derived laminar burning velocities are in good agreement with predictions based on recently developed H_2/CH_4 mechanisms, namely; San Diego, Konnov and Aramco2.0 kinetics. Although the agreement between simulations and experiment becomes poorer for rich-pure hydrogen flames, predictions remain within the limits of uncertainty in the experimental results.

CRediT authorship contribution statement

Marwaan AL-Khafaji: Visualization, Validation, Methodology, Formal analysis, Data curation, Investigation, Writing - original draft. **Junfeng Yang:** Conceptualization, Review, Supervision, Funding acquisition, Resources. **Alison S. Tomlin:** Writing – review & editing, Supervision, Methodology, Investigation. **Harvey M. Thompson:** Writing, Review, Supervision. **Gregory de Boer:** Supervision. **Kexin Liu:** Conceptualization. **Mohamed E. Morsy:** Methodology, Validation, Review, Supervision.

Declaration of Competing Interest

The authors declare that they have no known competing financial interests or personal relationships that could have appeared to influence the work reported in this paper.

Data availability

Data will be made available on request.

Acknowledgments

Mr. M. AL-Khafaji acknowledges the Republic of Iraq/ Ministry of Electricity/ State Company of Electricity Production- North region for sponsoring the PhD scholarship. Dr. J. Yang and Dr. M.E. Morsy thank EPSRC (Grant No. EP/W002299/1) for financial support. The authors would like to acknowledge valuable discussions with Prof. Derek Bradley and Dr. Christian Michelbach.

Appendix A

(See Table A1, Table A2, Table A3, Table A4).

References

[1] Nilsson EJK, van Sprang A, Larfeldt J, Konnov AA. The comparative and combined effects of hydrogen addition on the laminar burning velocities of methane and its blends with ethane and propane. Fuel 2017;189:369–76.
[2] Ravi S, Morones A, Petersen EL, and Güthe F. Effects of hydrogen addition on the flame speeds of natural gas blends under uniform turbulent conditions. In: Proceedings of the ASME Turbo Expo: Turbine Technical Conference and Exposition. Volume 4A: Combustion, Fuels and Emissions. Montreal, Quebec, Canada. June 15–19, 2015, paper GT2015-42903, V04AT04A066; 11 pages.
[3] Petersen EL, Kalitan DM, Simmons S, Bourque G, Curran HJ, Simmie JM. Methane/propane oxidation at high pressures: Experimental and detailed chemical kinetic modeling. Proc Combust Inst 2007;31:447–54.
[4] Jackson GS, Sai R, Plaia JM, Boggs CM, Kiger KT. Influence of H2 on the response of lean premixed CH4 flames to high strained flows. Combust Flame 2003;132:503–11.
[5] Salzano E, Cammarota F, Di Benedetto A, Di Sarli V. Explosion behavior of hydrogen–methane/air mixtures. J Loss Prev Process Ind 2012;25:443–7.
[6] Chiesa P, Lozza G, Mazzocchi L. Using hydrogen as gas turbine fuel. J Eng Gas Turbines Power 2005;127:73–80.
[7] Sankaran R, Im HG. Effects of hydrogen addition on the markstein length and flammability limit of stretched methane/air premixed flames. Combust Sci Technol 2006;178:1585–611.
[8] Schefer RW, Wicksall DM, Agrawal AK. Combustion of hydrogen-enriched methane in a lean premixed swirl-stabilized burner. Proc Combust Inst 2002;29:843–51.
[9] Aung KT, Hassan MI, Faeth GM. Flame stretch interactions of laminar premixed hydrogen/air flames at normal temperature and pressure. Combust Flame 1997;109:1–24.
[10] Huzayyin AS, Moneib HA, Shehatta MS, Attia AMA. Laminar burning velocity and explosion index of LPG–air and propane–air mixtures. Fuel 2008;87:39–57.
[11] Hu E, Huang Z, He J, Jin C, Zheng J. Experimental and numerical study on laminar burning characteristics of premixed methane–hydrogen–air flames. Int J Hydrogen Energy 2009;34:4876–88.
[12] Wu F, Liang W, Chen Z, Ju Y, Law CK. Uncertainty in stretch extrapolation of laminar flame speed from expanding spherical flames. Proc Combust Inst 2015;35:663–70.
[13] Chen Z. On the accuracy of laminar flame speeds measured from outwardly propagating spherical flames: Methane/air at normal temperature and pressure. Combust Flame 2015;162:2442–53.
[14] Fairweather M, Ormsby MP, Sheppard CGW, Woolley R. Turbulent burning rates of methane and methane–hydrogen mixtures. Combust Flame 2009;156:780–90.

[15] Hu E, Huang Z, Zheng J, Li Q, He J. Numerical study on laminar burning velocity and NO formation of premixed methane–hydrogen–air flames. Int J Hydrogen Energy 2009;34:6545–57.
[16] Sung CJ, Huang Y, Eng JA. Effects of reformer gas addition on the laminar flame speeds and flammability limits of n-butane and iso-butane flames. Combust Flame 2001;126:1699–713.
[17] Yu G, Law CK, Wu CK. Laminar flame speeds of hydrocarbon + air mixtures with hydrogen addition. Combust Flame 1986;63:339–47.
[18] Mandilas C, Ormsby MP, Sheppard CGW, Woolley R. Effects of hydrogen addition on laminar and turbulent premixed methane and iso-octane–air flames. Proc Combust Inst 2007;31:1443–50.
[19] Hu E, Huang Z, He J, Zheng J, Miao H. Measurements of laminar burning velocities and onset of cellular instabilities of methane–hydrogen–air flames at elevated pressures and temperatures. Int J Hydrogen Energy 2009;34:5574–84.
[20] Okafor EC, Hayakawa A, Nagano Y, Kitagawa T. Effects of hydrogen concentration on premixed laminar flames of hydrogen–methane–air. Int J Hydrogen Energy 2014;39:2409–17.
[21] Wang Q, Mei XH, Wei ZY, Zhao CY, Zhang Y. Experimental investigation of transient ignition dynamics of hydrogen enriched methane diffusion impinging flames. Fuel 2021;290:120027.
[22] Hassan MI, Aung KT, Faeth GM. Measured and predicted properties of laminar premixed methane/air flames at various pressures. Combust Flame 1998;115:539–50.
[23] Iijima T, Takeno T. Effects of temperature and pressure on burning velocity. Combust Flame 1986;65:35–43.
[24] Milton BE, Keck JC. Laminar burning velocities in stoichiometric hydrogen and hydrogen/hydrocarbon gas mixtures. Combust Flame 1984;58:13–22.
[25] Verhelst S, Woolley R, Lawes M, Sierens R. Laminar and unstable burning velocities and Markstein lengths of hydrogen–air mixtures at engine-like conditions. Proc Combust Inst 2005;30:209–16.
[26] Bradley D, Lawes M, Liu K, Verhelst S, Woolley R. Laminar burning velocities of lean hydrogen–air mixtures at pressures up to 1.0 MPa. Combust Flame 2007;149:162–72.
[27] Bechtold JK, Matalon M. Hydrodynamic and diffusion effects on the stability of spherically expanding flames. Combust Flame 1987;67:77–90.
[28] Bradley D. Instabilities and flame speeds in large-scale premixed gaseous explosions. Philosoph Transact Royal Soc London Series A: Math Phys Eng Sci 1999;357:3567–81.
[29] Xie Y, Morsy ME, Li J, Yang J. Intrinsic cellular instabilities of hydrogen laminar outwardly propagating spherical flames. Fuel 2022;327:125149.
[30] Konnov AA, Mohammad A, Kishore VR, Kim NI, Prathap C, Kumar S. A comprehensive review of measurements and data analysis of laminar burning velocities for various fuel+air mixtures. Prog Energy Combust Sci 2018;68:197–267.
[31] Sen U, Gangopadhyay T, Bhattacharya C, Mukhopadhyay A, Sen S. Dynamic characterization of a ducted inverse diffusion flame using recurrence analysis. Combust Sci Technol 2018;190:32–56.
[32] Bradley D, Hicks RA, Lawes M, Sheppard CGW, Woolley R. The measurement of laminar burning velocities and markstein numbers for iso-octane–air and iso-octane–n-heptane–air mixtures at elevated temperatures and pressures in an explosion bomb. Combust Flame 1998;115:126–44.
[33] Gu XJ, Haq MZ, Lawes M, Woolley R. Laminar burning velocity and Markstein lengths of methane–air mixtures. Combust Flame 2000;121:41–58.
[34] Williams FA, Seshadri K, and Catolica R, The San Diego Mechanism, Chemical-Kinetic Mechanisms for Combustion Applications, 2015, https://web.eng.ucsd.edu/mae/groups/combustion/mechanism.html.
[35] Zhang Y, Fu J, Shu J, Xie M, Liu J. A chemical kinetic investigation of laminar premixed burning characteristics for methane-hydrogen-air mixtures at elevated pressures. J Taiwan Inst Chem Eng 2020;111:141–54.
[36] Zhang P, Zsély IG, Papp M, Nagy T, Turányi T. Comparison of methane combustion mechanisms using laminar burning velocity measurements. Combust Flame 2022;238:111867.
[37] Bradley D, Lawes M, Mumby R, Ahmed P. The stability of laminar explosion flames. Proc Combust Inst 2019;37:1807–13.
[38] Mumby RD, Experimental characterisation of fuel blends, [Doctoral dissertation, University of Leeds] 2016.
[39] Bradley D, Lawes M, Morsy ME. Measurement of turbulence characteristics in a large scale fan-stirred spherical vessel. J Turbul 2019;20:195–213.
[40] Bradley D, Lawes M, Morsy ME. Flame speed and particle image velocimetry measurements of laminar burning velocities and Markstein numbers of some hydrocarbons. Fuel 2019;243:423–32.
[41] Shehata MMAO, New Fuels, Flame quenching and DDT, [Doctoral dissertation, University of Leeds] 2019.
[42] Bradley D, Lau AKC, Lawes M, Smith FT. Flame stretch rate as a determinant of turbulent burning velocity. Philosoph Transact Royal Soc London Series A: Phys Sci Eng 1992;338:359–87.
[43] Williams FA. Combustion theory: the fundamental theory of chemically reacting flow systems, 2nd ed. (Combustion, Science, and Engineering series), Menlo Park, Calif, Benjamin/Cummings Pub. Co.; 1985.
[44] Bradley D, Gaskell PH, Gu XJ. Burning velocities, markstein lengths, and flame quenching for spherical methane-air flames: A computational study. Combust Flame 1996;104:176–98.
[45] Morsy ME. Studies of Laminar and Turbulent Combustion Using Particle Image Velocimetry, [Doctoral dissertation, University of Leeds] 2019.
[46] Morley C. Gaseq: A chemical equilibrium program for Windows; 2005.
[47] Kelley AP, Law CK. Nonlinear effects in the extraction of laminar flame speeds from expanding spherical flames. Combust Flame 2009;156:1844–51.
[48] Göttgens J, Mauss F, Peters N. Analytic approximations of burning velocities and flame thicknesses of lean hydrogen, methane, ethylene, ethane, acetylene. Proc Combust Inst 1992;24:129–35.
[49] Bradley D, Lawes M, Morsy ME. Combustion-induced turbulent flow fields in premixed flames. Fuel 2021;290:119972.
[50] Bradley D, Shehata M, Lawes M, Ahmed P. Flame extinctions: Critical stretch rates and sizes. Combust Flame 2020;212:459–68.
[51] Huo J, Saha A, Ren Z, Law CK. Self-acceleration and global pulsation in hydrodynamically unstable expanding laminar flames. Combust Flame 2018;194:419–25.
[52] Mansour MS. Fundamental study of premixed combustion rates at elevated pressure and temperature, [Doctoral dissertation, University of Leeds] 2010.
[53] Morsy ME, Yang J. The instability of laminar methane/hydrogen/air flames: Correlation between small and large-scale explosions. Int J Hydrogen Energy 2022;47:29959–70.
[54] Zhao H, Wang J, Bian Z, Cai X, Li X, Huang Z. Onset of cellular instability and self-acceleration propagation of syngas spherically expanding flames at elevated pressures. Int J Hydrogen Energy 2019;44:27995–8006.
[55] Bradley D, Sheppard CGW, Suardjaja IM, Woolley R. Fundamentals of high-energy spark ignition with lasers. Combust Flame 2004;138:55–77.
[56] Qin X, Kobayashi H, Niioka T. Laminar burning velocity of hydrogen–air premixed flames at elevated pressure. Exp Therm Fluid Sci 2000;21:58–63.
[57] Aung KT, Hassan Faeth MI. Effects of pressure and nitrogen dilution on flame/stretch interactions of laminar premixed H2/O2/N2 flames. Combust Flame 1998;112:1–15.
[58] Sun CJ, Sung CJ, He L, Law CK. Dynamics of weakly stretched flames: quantitative description and extraction of global flame parameters. Combust Flame 1999;118:108–28.
[59] Law CK, Sung CJ. Structure, aerodynamics, and geometry of premixed flamelets. Prog Energy Combust Sci 2000;26:459–505.
[60] Varea E, Beeckmann J, Pitsch H, Chen Z, Renou B. Determination of burning velocities from spherically expanding H2/air flames. Proc Combust Inst 2015;35:711–9.
[61] ANSYS CHEMKIN 21.0, ANSYS Reaction Design: San Diego, 2021.